Cerebellar interneuron activity is triggered by reach endpoint during learning of a complex locomotor task

Andry Andrianarivelo[1], Heike Stein[2], Jeremy Gabillet[1], Clarisse Batifol[1], Abdelali Jalil[1], N Alex Cayco Gajic[2], and Michael Graupner[1]

[1]Université Paris Cité, SPPIN - Saints-Pères Paris Institute for the Neurosciences, CNRS, Paris 75006, France
[2]Département d'Études Cognitives, École Normale Supérieure, Université Paris Sciences et Lettres, Paris 75005, France

Corresponding author email address:
michael.graupner@u-paris.fr

Abstract

Locomotion in complex environments depends on the precise timing and active control of single paw movements in order to adapt steps to surface structure and coordinate paws. Such motor control crucially depends on the cerebellum. In turn, cerebellar activity is reported to reflect limb movement kinematics, but how precise action timing in complex environments is controlled by the cerebellar circuit is currently unknown. To address this question, we developed LocoReach: a new task which combines continuous and discrete aspects of motor control by requiring mice to walk on a runged treadmill, where each step involves reaching for the next rung. Over several days of learning, mice became increasingly proficient at LocoReach, so that they made fewer, longer strides with faster swings and fewer missteps. We assessed the cerebellar role during LocoReach learning through pharmacological inhibition as well as real-time optogenetic inhibition of cerebellar activity and electrophysiological recordings of molecular layer interneurons (MLIs), as they are thought to control the timing and gain of the cerebellar cortical output. Inhibiting cerebellar output during the swing phase of a specific paw led to shorter swings of this paw. When analyzing behaviorally-evoked responses in MLIs, we found sharp changes in activity around paw-specific transitions from swing to stance and vice versa. While most MLIs in the left simplex were preferentially modulated by the reach endpoint of the front left paw, a large proportion of cells additionally showed activity variations related to other paws or even multiple paws. Stronger firing rate modulations reflected longer strides made over learning, consistent with previous reports highlighting the role of the intermediate cerebellum in controlling reach endpoint precision. Our results provide the first demonstration that cerebellar inhibitory signals are tuned to specific events in the step cycle which can act as a powerful mechanism for the precise control of paw placements.

Introduction

Precise control of movements during locomotion is essential for maintaining balance and preventing falls in challenging environments, such as uneven or unstable surfaces or when navigating obstacles. The cerebellum plays an important role during such tasks by integrating sensorimotor information allowing it to predict the consequences of motor commands and to make adjustments in real time to ensure that movements are accurate and well-timed (Morton and Bastian 2006). Locomotion in challenging environments is highly discontinuous with momentary and cyclically changing demands on motor output precision. How the nature of such movements interacts with cerebellar activity remains elusive.

During skilled movements like reaching to retrieve food pellets, the intermediate cerebellum helps to achieve precision by influencing the kinematics of the reach (Becker and Person, 2019) possibly through prediction of reach kinematics encoded by population activity (Calame et al., 2023). During locomotion, cerebellar activity has been linked to kinematic variables of individual limbs (Becker and Person, 2019; Heiney et al., 2014; Hewitt et al., 2015; Hewitt et al., 2011; Pasalar et al., 2006; Vinueza Veloz et al., 2015), coordination across limbs (Darmohray et al., 2019; Vinueza Veloz et al., 2015), and whole-body coordination (Machado et al., 2015) or state variables (Lanore et al., 2021). For locomotion on non-flat surfaces such as a horizontal ladder, Purkinje cells in the intermediate cerebellum show step-related rhythmic activity (Marple-Horvat and Criado, 1999).

Cerebellar motor control relies on signal processing in the cerebellar cortical microcircuit, where sensorimotor information is integrated by Purkinje cells (PCs), which constitute the sole output of the cerebellar cortex. The precision of PCs' spike output timing and gain is controlled by molecular layer interneurons (MLIs), both cells receiving excitatory inputs from parallel fibers, providing robust feed-forward inhibition (Arlt and Häusser, 2020; Barmack and Yakhnitsa, 2008; Duguid et al., 2012; Eccles et al., 1967; Mittmann et al., 2005). In turn, MLI mediated inhibition controls the timing and tunes the kinematics of motor output (Heiney et al., 2014). Previous studies have shown that MLI firing rates increase globally during locomotion compared to rest (Bao et al., 2020; Jelitai et al., 2016; Ozden et al., 2012). However, the encoding of locomotor cycle events and motor parameters by MLIs is still unknown.

To elucidate the role of MLIs in locomotor control and learning, we investigated MLI activity during skilled limb movements and locomotor learning in mice using a novel task: LocoReach. This task combines walking on a motorized, runged treadmill with reaching movements and allows for simultaneous neural recordings. Through pharmacological and closed-loop optogenetic inhibition, we demonstrated the involvement of the cerebellar lobule simplex in LocoReach task execution. We next performed single-cell electrophysiological recordings of MLIs during the LocoReach task. We found that the majority of MLIs encode swing and stance phases with precisely timed firing rate changes related to stride events, especially at transitions between swing and stance. We observed that MLI engagement increased linearly with step length as mice adapted their locomotion. We found that a substantial fraction of MLIs were selective for transitions of more than one paw, even when using a sparsity-constrained model to control for correlations between different paws. Our results reveal specialized MLI firing patterns during locomotion, with precise modulation of activity in relation to events in the step cycle when motor control demands are highest. Our findings shed a light on the contribution of MLIs activity during locomotor adaptation that could play a central role for sculpting cerebellar output to achieve motor precision and learning.

Results

LocoReach task allows for finely resolved paw movement analysis in a complex environment

We developed a motorized treadmill with regularly spaced rungs to study locomotor learning in head-fixed mice. Naïve mice were head-fixed on top of a treadmill with regularly spaced rungs and a constant baseline speed of 7.5 cm/s was imposed during the motorization period. Mice had to rely on whisker-guided walking for LocoReach as the task is implemented in complete darkness. A mirror mounted inside the wheel at 45° allowed both side and bottom views to be captured using infrared illumination and a high-speed camera (Fig. 1A). We tracked all four paws (front right - FR, front left - FL, hind right - HR, hind left - HL) in the bottom view with high accuracy (Fig. 1B,C; see Materials and Methods for more details).

To classify each paw trajectory time series into swing (paw in the air) and stance (paw resting on rung) phases, we developed a custom routine based on the difference between paw- and wheel speed and taking into account the paw-rung distance (Fig. 1D, see Methods for criteria). Comparable to freely walking mice at slow walking speeds similar to the imposed speed, paws spent larger fractions of the total stride time in the stance compared to swing phase (all mice and FL paw : swing duration $[0.055, 0.09, 0.14]$ s and stance duration $[0.075, 0.205, 0.365]$ s for $[25, 50, 75]$th percentile) (Fig. 1E, Machado et al., 2015). In contrast to walking on a flat surface however, swing- and stance durations were highly variable due to irregular paw movements on the runged wheel and the paw could sometimes miss the rung at the end of the swing phase, both effects owing to the difficulty of the task because of the rungs. Paw position corrections in particular lead to short stances (< 0.1 s) and swings (< 0.05 s) (Fig. 1E). Miss steps were characterized by multiphasic paw speed profiles (swings with diagonal stripes in Fig. 1D) from the slow-down at the expected paw landing time and the acceleration of the subsequent corrective movement. The miss steps give us a means to quantify paw reaching precision during learning.

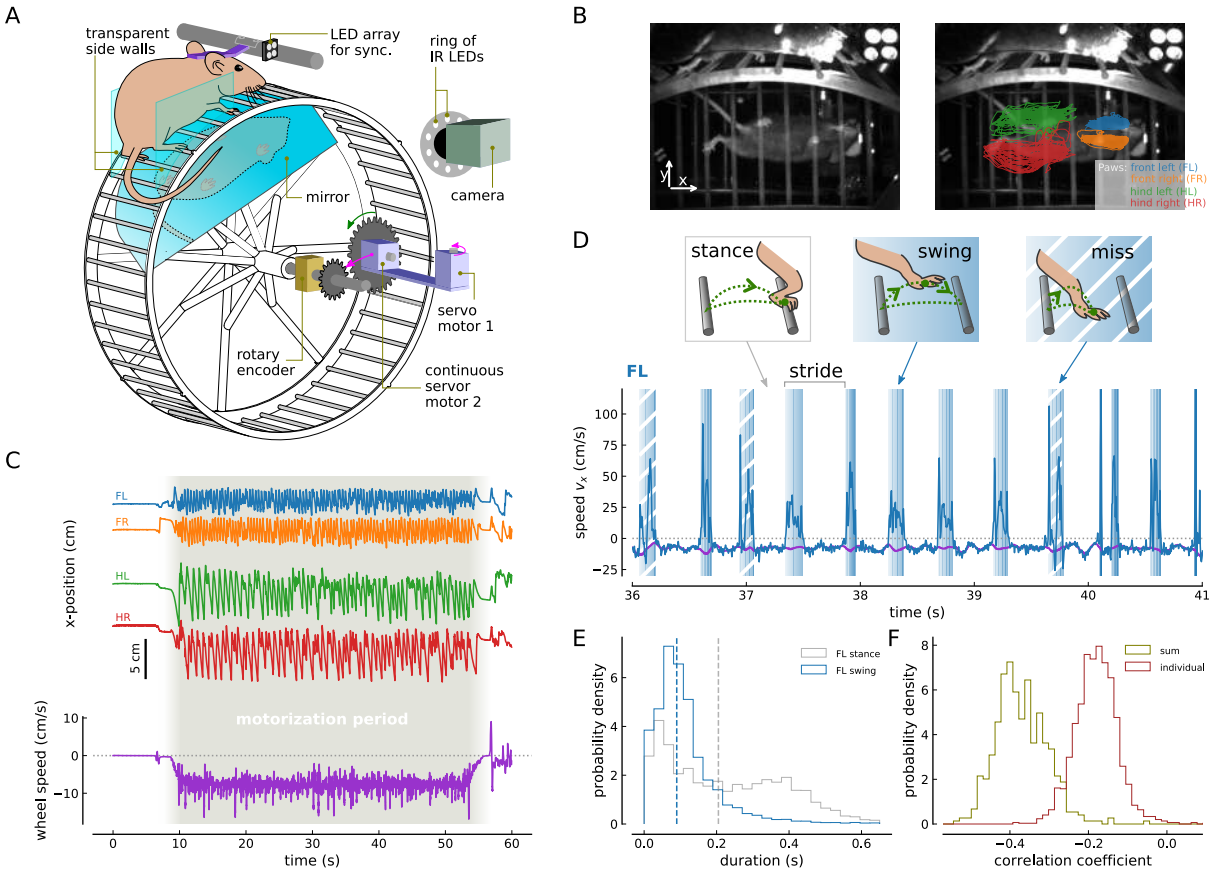

Figure 1: LocoReach is a challenging locomotor task that allows for the analysis of paw specific stepping patterns during locomotion in a complex environment. (**A**) Schematic of the LocoReach setup. Head-fixed mice were placed on top of a runged treadmill with regularly spaced rungs in complete darkness. Mice were illuminated with infrared light. Bottom and side view of the animal were filmed with a high-speed camera (200 fps) through a 45°-inclined mirror under the wheel. During motorization, a servo motor (1) moved in a gear and a continuous servo motor (2) imposed a constant speed. Wheel angluar position was tracked with a rotary encoder. (**B**) Video frames showing a mouse walking on the wheel (left), and with overlayed FL (blue), FR (orange), HL (green) and HR (red) paw trajectories of one recording (right). (**C**) Individual paw x-positions (in the direction of forward locomotion, top) and wheel speed (purple, bottom) vs time during a sample recording. The motorization period (shaded region) started at 7 s with a smooth acceleration, followed by a constant speed period, $[10, 52]$ s, and a deceleration. (**D**) Wheel (purple) and FL paw speed vs time. Swing (changed regions) and stance phases were identified based on the speed difference between the two. Swing and stance phase together constitute the stride of a single paw. Miss steps occurred when the paw did not land directly on a rung and had to correct its position, leading to a multi-phasic paw speed profile (diagonally-striped swings). (**E**) Swing and stance duration histograms. Dashed lines correspond to median at 0.09 s for swing and 0.205 s for stance. (**F**) Correlation coefficient distributions between wheel and paw speeds. Wheel speed is correlated with the sum of all four relative paw speeds (olive), and the individual relative paw speeds (brown). Distributions in E and F comprise all recordings ($R = 492$) from all mice ($N = 11$).

The imposed wheel speed was not rigid but was modulated by the movement and the force exerted by the animal (Fig. 1C). In particular, swings of all four paws are accompanied by a backward acceleration (in negative x-direction) of the wheel due to the counterforce of paw advancement (Fig. 1C,D,F). As a consequence, the wheel speed exhibits a stronger negative correlation with the sum of all four paws speeds compared to the individual paw speeds (Fig. 1F). The variations of the imposed wheel speed thereby reflects the overall movement state of the animal, *i.e.*, the forward movements of all four paws negatively impacts the wheel speed.

LocoRungs was inspired by a task for which the cerebellar involvement has been demonstrated (Vinueza Veloz et al., 2015), while additionally providing access to individual paw trajectories allowing for highly refined behavioral analysis of locomotor dynamics and precision. The head-fixed positioning of mice furthermore opened the possibility for neural recordings during task execution (see below). Together, LocoReach promises novel insights into the intricate interplay between locomotor behavior in complex environments and brain activity.

Mice refine their step kinematics and paw coordination over learning

To assess locomotor learning on the LocoReach apparatus, naïve, adult mice underwent single daily sessions of multiple recording trials for 8 to 10 days. By imposing a constant walking speed over multiple trials and sessions, we aimed to quantify changes in locomotor parameters and precision for otherwise constant task conditions. Mice were habituated to the setup and the head-fixed position without exposure to the rungs prior to LocoReach learning. Mice could walk freely and self-paced outside the motorization period.

First, we asked how single paw behavior changed over the course of the learning protocol and found that mice showed significant changes in multiple walking parameters across sessions and trials. Specifically, the stride number (number of swings) across trials and across sessions decreased significantly (Fig.2A), which occurred in parallel with an increase in the swing length across trials and sessions (Fig.2B). Resolving swing length for individual paws showed that execution of longer strides occurs for all paws across trials and sessions (Fig. 2C). Fewer and longer strides allowed mice to cover the same distance later during trials as well as sessions.

The stride frequency reduction across sessions was achieved mostly by increasing the duration of the stance phase (Fig. 2D), consistent with what has been reported for walking on flat surfaces for mice and flies (Gonçalves et al., 2022). Swing duration decreased slightly across sessions (Fig. 2D) while swing speed increased to execute the longer strides (Fig. 2E). Also the precision of the strides increased across sessions as quantified by the decrease in the fraction of miss steps (Fig. 2F). Together, we see fewer and longer strides, longer stride durations, and less miss steps demonstrating that head-fixed mice walking on the treadmill with rungs exhibit the same improvements in locomotor performance as freely walking mice on the Erasmus Ladder (Vinueza Veloz et al., 2015).

We next asked whether regularity of single paw movements and inter-paw coordination changed during the protocol by computing the relative timing of front paw swing phases. Two changes were apparent across trials and across sessions: (i) the swing duration of the FL paw became less variable, and (ii) the swing phase of the front right paw started more consistently at 50 % of the front right stride cycle later in training, as illustrated in the Hildebrand plots in Fig. 2G. The regularity of the FL swing phase was quantified by the interquartile range of the stance onset time which decreases over sessions (Fig. 2G,H). The entrainment of the FR paw with the FL can be observed in the median swing-onset time which indicates that FR and FL develop a 50 % phase offset over learning as evidence of more coordinated movements (Fig. 2H).

In summary, the improvements in motor performance, precision, regularity and coordination indicate that mice were adapting to the wheel speed and rung spacing and became more precise in their movements. The changes in the walking parameters are highly interdependent, *e.g.*, swing speed is positively correlated with stride length and stance duration, while it is negatively correlated with stride number and fraction of miss steps (Fig. 2I). The correlations between FL paw kinematic variables highlight the complexity of locomotion where individual paw kinematic variables are interdependent signatures of an improved gait pattern.

Cerebellar lobulus simplex inactivation impacts locomotor performance

Several studies report the implication of the intermediate cerebellum in locomotor adaption (Darmohray et al., 2019) and reaching (Becker and Person, 2019). We next silenced activity in the lobulus simplex to determine its causal implication in the the LocoReach task, which combines both locomotor and reaching

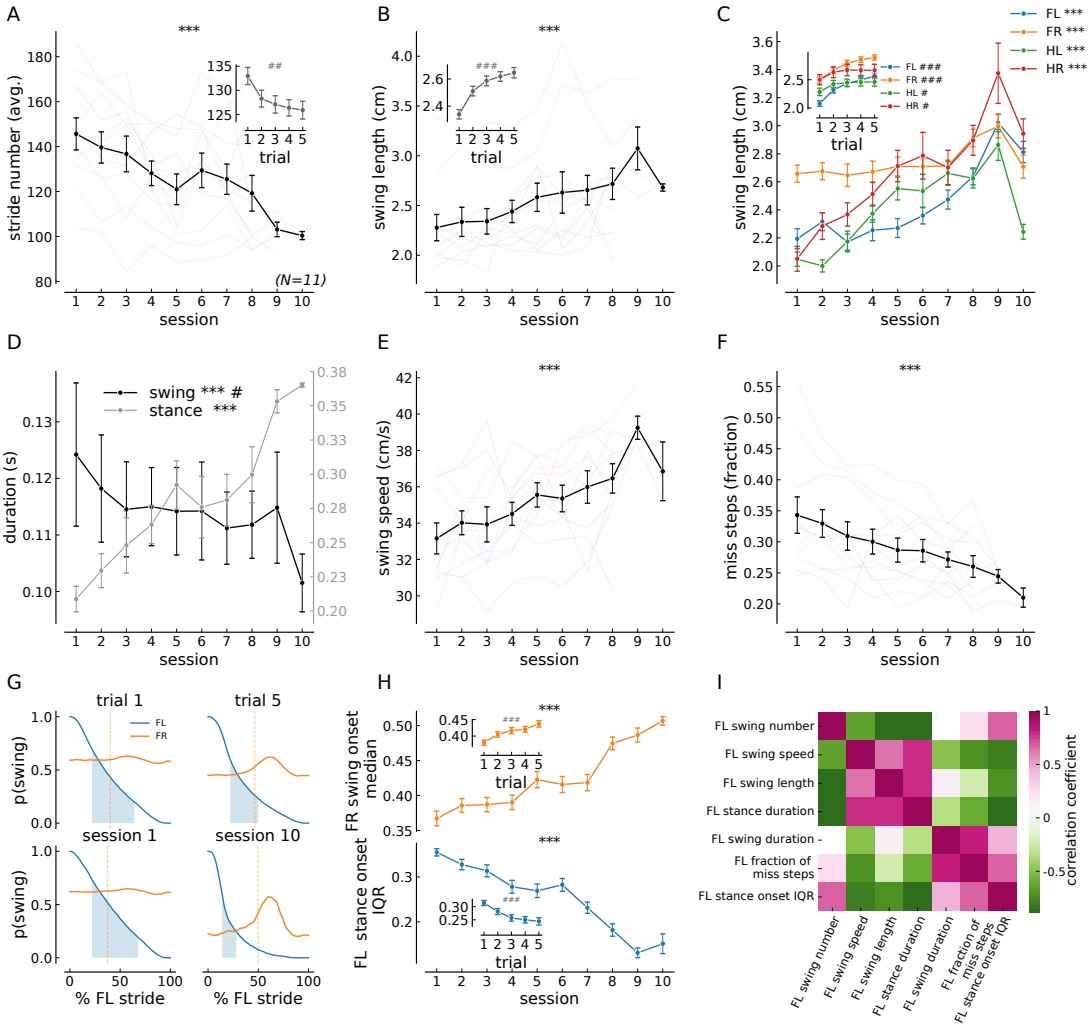

Figure 2: Behavioral learning occurs across trials and sessions. The mean of single paw behavioral measures are shown over sessions and trials (insets), such as : (**A**) stride number of all paws (session effect: $C = -3.831$, $p < 0.0001$, trial effect: $C = -1.011$, $p = 0.002$), (**B**) swing length for all paws (session effect :$C = 0.069$, $p < 0.0001$, trial effect: $C = 0.054$, $p < 0.0001$), (**C**) swing length for individual paws (FL, session effect: $C = 0.061$, $p < 0.0001$, trial effect: $C = 0.097.33$, $p < 0.0001$; FR, session effect: $C = 0.0240$, $p < 0.0001$, trial effect: $C = 0.066$, $p < 0.0001$; HL, session effect: $C = 0.088$, $p < 0.0001$, trial effect: $C = 0.02$, $p = 0.042$; HR, session effect: $C = 0.104$, $p < 0.0001$, trial effect: $C = 0.032$, $p = 0.012$), (**D**) swing and stance duration for all paws (swing duration - session effect: $C = -0.001$, $p < 0.0001$, trial effect: $C = 0.001$, $p = 0.015$; stance duration - session effect: $C = 0.013$, $p < 0.0001$, trial effect: $C = 0.001$, $p = 0.100$), (**E**) swing speed for all paws (session effect: $C = 0.550$, $p < 0.0001$, trial effect: $C = 0.047$, $p = 0.421$), (**F**) fraction of miss steps for all paws (session effect: $C = -0.012$, $p < 0.0001$, trial effect: $C = -0.001$, $p = 0.328$). Measures over trials are shown as insets in panels where the trial effect is significant. (**G**) Average Hildebrand plots aligned to the FL swing onset, representing the probability of swing for FL (blue) and FR paw (orange) paw for the first trial (upper left), fifth trial (upper right), first session (lower left) and last session of training (lower right) for all animals. Blue shaded area represent the 25-75th interquartile range (IQR) for the FL paw stance onset time, and the vertical orange line shows the median swing onset time for FR paw. (**H**) Median swing onset time of FR paw relative to FL swing onset (top, session effect: $C = 0.013$, $p < 0.0001$, trial effect: $C = 0.012$, $p < 0.0001$). Stance onset time IQR of FL paw relative to FL swing onset (bottom, session effect: $C = -0.021$, $p < 0.0001$, trial effect: $C = -0.014$, $p < 0.0001$). Averages across animals are shown over sessions and over trials. (**L**) Correlation matrix between behavioral parameters. Pearson correlation coefficient heat-map for FL paw. Colors represent correlation coefficient with p-value < 0.05 ($N = 11$). In panels (A)-(F),(H), Data are presented as mean $\pm$ SEM. Black lines show group averages and pale, colored lines show individual animals. Statistical significance of effects was determined using a Linear Mixed Model. The regression coefficient (C) and corresponding p-value are reported for each effect tested. $^*p < 0.05$, $^{**}p < 0.01$, $^{***}p < 0.0001$ effect of sessions. $\#p < 0.05$, $\#\#p < 0.01$, $\#\#\#p < 0.0001$ trial effect.

components. We took two approaches for silencing activity, muscimol infusion and temporally precise, closed-loop optogenetic inhibition.

For the pharmacological interference, fluorophore-conjugated muscimol or saline were perfused in 16 mice 30 min before each session. Muscimol infused animals performed more strides to cover the same distance compared to the saline group (Fig. A.1B,C), while there was no difference in the fraction of miss steps between the muscimol- and saline-infused mice. Therefore, muscimol inactivation of the lobulus simplex affected single paw kinematics, but not paw precision during LocoReach adaptation.

Becker and Person, 2019 showed that interposed nucleus activation causes hypometric reaches. We wondered whether we can curtail steps by inhibiting lobulus simplex output, which corresponds to removing inhibition from the interposed nucleus, during the swing phase. To answer this question, we performed closed-loop interference experiments to inhibit cerebellar activity during swing phases of the front left (FL) paw (Fig. 3A). For that purpose, a blue-light sensitive inhibitory option (GtACR2, Forli et al., 2018; Govorunova et al., 2015) was expressed in cerebellar cortical neurons (Fig. 3C). Using the speed of the FL paw, which was evaluated in real time, blue light was delivered specifically during the FL swing phase (Fig. 3A,B). Opsin-expressing animals exhibited significantly shorter FL paw swing lengths during the first three sessions compared to the control group (exposed to the same manipulations but expressing tdTomato, Fig. 3D), while the swing lengths of the other four paws remained unchanged (Fig. 3D). As for muscimol infusions, no differences emerged in the fraction of miss-steps between opsin- and control mice (Fig. 3E). Notably, the FR paw stance onset time IQR was increased in perturbed animals, again lasting for the initial 3 sessions (Fig. 3F). This result points to a disrupted coordination between FL and FR paw.

In summary, temporally-specific inhibition of cerebellar lobulus simplex during FL swing phases reduced FL swing length and thereby disrupted front paw coordination. This results demonstrates the implication of lobulus simplex in the online control of limb kinematics and coordination during skilled locomotion similar to skilled reaches (Becker and Person, 2019; Calame et al., 2023). Interestingly, mice adapted to the predictable optogenetic stimulation after 4 sessions exhibiting no difference to the control group (see discussion).

Molecular layer interneurons exhibit rich firing rate dynamics during LocoReach task

It has been reported previously that molecular layer interneurons increase their average firing rate during locomotion epochs (Jelitai et al., 2016; Ozden et al., 2012). To study their implication at a step-cycle resolved time-scale during the LocoReach task, we performed loose cell-attached recordings in the left lobulus simplex of the cerebellar cortex providing access to the spike output of single MLIs. These measurements were performed in transgenic animals expressing GCaMP6f in ~ 50 % of the MLIs and allowing for visually guided electrode approaches in a majority of the recordings (Fig. 4A,B).

Despite the fact that animals were awake and actively behaving, stable recordings at the transition from rest to locomotion (Fig. 4C,D), during the motorization period, and even across multiple trials provided access to the spike output of single MLIs during an entire behavioral session (Fig. 4C-G; total: 64 MLIs in 267 trials from $N = 11$ mice). We recorded from different MLIs across sessions from the same animal resulting in $3 - 10$ cells recorded in total per animal during the learning period (Fig. 4H). We further confirmed the MLI identity of the recorded cells and excluded putative Purkinje cells through clustering based on the cell's electrophysiological signature including spike waveform, spike autocorrelogram, existence of complex spikes, firing rate, and spike-count variability (Fig. A.2).

As expected, locomotor activity was accompanied by a significant increase in MLI firing rate (Fig. 4H; baseline FR $[12.7, 20.2, 28.8]$ spk/s, walking FR $[28.1, 38.4, 50.6]$ spk/s for $[25, 50, 75]$th percentile). The variability of inter-spike intervals was equally high during rest- and locomotor periods (Fig. 4I; baseline CV $[0.74, 0.95, 1.12]$, walking CV $[0.83, 0.94, 1.10]$ for $[25, 50, 75]$th percentile). We next asked whether the rich temporal dynamics of the firing rate during the locomotor period was related to measured task variables. As shown above, the wheel speed reflects the overall locomotor state of the animal including contributions from the individual movements of all four paws. Indeed, we found that the firing rate of more than half of the cells is moderately positively or negatively correlated with the wheel speed (Pearson correlation with $p < 0.05$ for $140/267$ recordings; Fig. 4J).

Stride-related firing rate modulations linked to swing- and stance onset

The observation that the wheel speed is correlated with MLI activity of many cells during locomotion (Fig. 4H) raised the question whether the swing-stance cycle of individual paws modulates MLI activity. The cerebellar simplex projects to the anterior interposed nucleus, where cells exhibit reach-endpoint

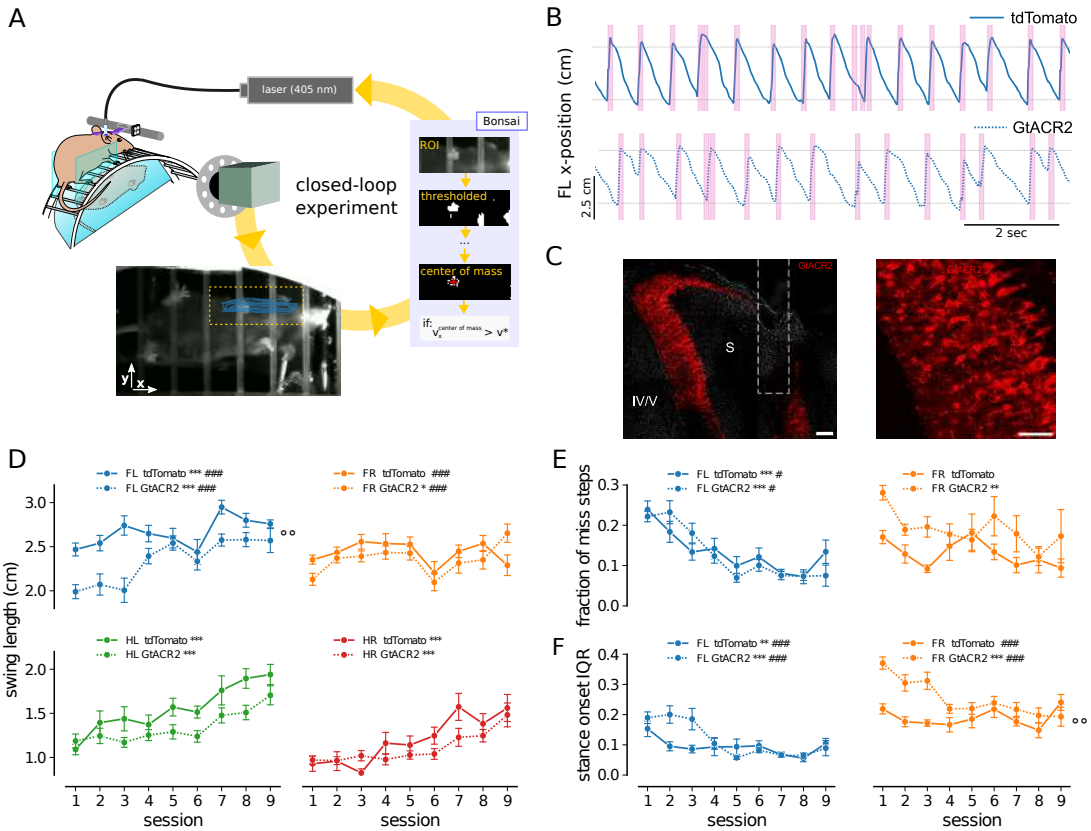

Figure 3: Closed-loop inactivation of lobule simplex affects swing length and paw coordination. (**A**) Schematic of close-loop inactivation of lobule simplex cerebellar cortex. Video recording stream was processed in real-time in Bonsai (Lopes et al., 2015) to extract FL paw center of mass position and speed across frames. Whenever paw speed exceeded a threshold, which was adjusted to identify swing onset, the laser was triggered. (**B**) FL paw (blue) x-position over time during a sample period of a single trial for a tdTomato (top, full line) and a GtACR2-injected animal (bottom, dashed line). Swing-start triggered blue laser activations (80ms duration, 30mW) are indicated by pink bars. (**C**) Photomicrograph showing expression of GtACR2-FusionRed in a coronal cerebellar section (left, scale bar: 100 μm). Dashed lines represent the tract of the optic fiber. Lobulus simplex (S) and lobule IV/V of the vermis are marked. Zoomed image of the expression of GtACR2-FusionRed showing expression in both MLIs and PCs (right scale bar: 50 μm). (**D**) Paw-resolved swing length of tdTomato (full lines, $N = 3$) and GtACR2 (dashed lines, $N = 5$) animals for FL (blue, tdTomato, session effect: $C = 0.042$, $p < 0.0001$, trial effect: $C = 0.101$, $p < 0.0001$; GtACR2, session effect: $C = 0.082$, $Z = 6.546$, $p < 0.0001$, trial effect: $C = 0.062$, $p = 0.012$, treatment effect: $C = 0.434$, $p = 0.009$), FR (orange, tdTomato, session effect: $C = -0.003$, $p = 0.752$, trial effect: $C = 0.081$, $p < 0.0001$; GtACR2, session effect: $C = 0.026$, $p = 0.018$, trial effect: $C = 0.049$, $p = 0.022$, treatment effect: $C = 0.137$, $p = 0.412$), HL (green, tdTomato, session effect: $C = 0.091$, $p < 0.0001$, trial effect: $C = 0.005$, $p = 0.759$; GtACR2, session effect: $C = 0.044$, $p < 0.0001$, trial effect: $C = -0.009$, , $p = 0.435$, treatment effect: $C = -0.053$, $Z = -0.260$, $p = 0.839$), and HR paws (red, tdTomato, session effect: $C = 0.083$, $p < 0.0001$, trial effect: $C = -0.018$, $p = 0.321$; GtACR2, session effect: $C = 0.047$, $p < 0.0001$, trial effect: $C = 0.004$, $p = 0.782$, treatment effect: $C = -0.04$, $p = 0.857$). (**E**) Fraction of miss steps of tdTomato (full lines) and GtACR2 animals (dashed lines) for FL (tdTomato, session effect: $C = -0.016$, $p < 0.0001$, trial effect: $C = -0.012$, $p = 0.045$; GtACR2, session effect: $C = -0.021$, $p < 0.0001$, trial effect: $C = -0.001$, $p = 0.81$, treatment effect: $C = 0.008$, $p = 0.838$) and FR paws (tdTomato, session effect: $C = -0.006$, $p < 0.061$, trial effect: $C = -0.011$, $p = 0.088$; GtACR2, session effect: $C = -0.012$, $p = 0.004$, trial effect: $C = -0.006$, $p = 0.490$, treatment effect: $C = -0.074$, $p = 0.230$). (**F**) Stance onset IQR of tdTomato and GtACR2 animals for FL (tdTomato, session effect: $C = -0.007$, $p = 0.004$, trial effect: $C = -0.018$, $p < 0.0001$; GtACR2, session effect: $C = -0.018$, $p < 0.0001$, trial effect: $C = -0.004$, $p = 0.422$, treatment effect: $C = -0.043$, $Z = -1.071$, $p = 0.284$) and FR paws (tdTomato, session effect: $C = 0.00$, $Z = 0.11$, $p = 0.912$, trial effect: $C = -0.024$, $p < 0.0001$; GtACR2, session effect: $C = -0.020$, $p < 0.0001$, trial effect: $C = -0.008$, $p = 0.166$, treatment effect: $C = -0.120$, $p = 0.008$). Data are presented as mean ± SEM over nine sessions. Statistical significance was determined by a Linear Mixed Model. The regression coefficient (C) and corresponding p-value are reported for behavioral parameters across sessions. $^{*}p < 0.05$, $^{**}p < 0.01$, $^{***}p < 0.0001$ effect of sessions. $\#p < 0.05$, $\#\#p < 0.01$, $\#\#\#p < 0.0001$ in-between trials effect. $^{\circ}p < 0.05$, $^{\circ\circ}p < 0.01$ treatment effect.

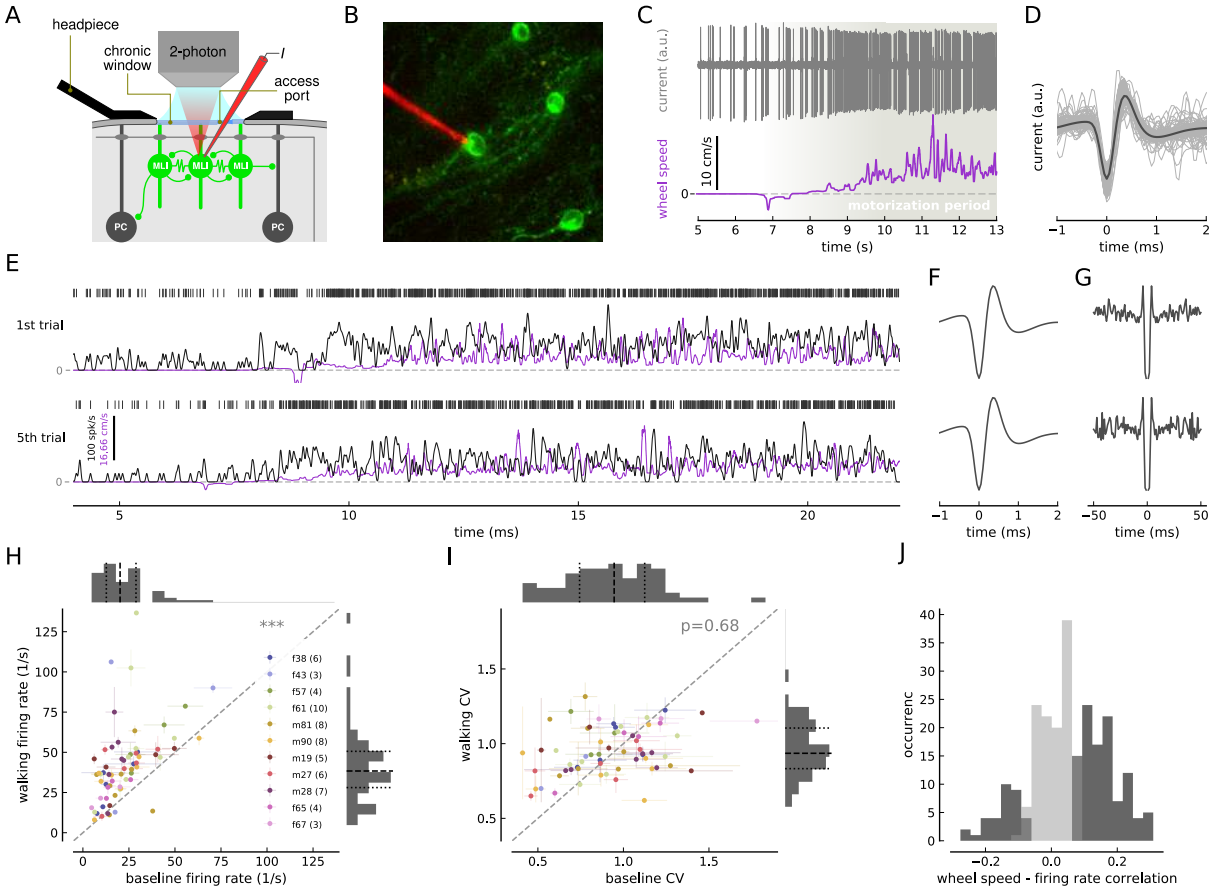

Figure 4: MLIs exhibit firing rate increase and rich dynamics during LocoReach task. (**A**) Schematic of *in vivo* loose cell-attached patch-clamp recordings of MLIs. GCAMP6f-expressing MLIs in transgenic mice were identified using two-photon microscopy through a chronic window and targeted through a silicone access port with a patch pipette loaded with Alexa 594. (**B**) *In vivo* two-photon micrograph of a patch pipette during a recording from a GCaMP6f-expressing MLI (scale bar 25 μm). (**C**) Wheel speed (violet) and example raw, electrophysiological trace (top, grey, high-pass filtered) of a loose-patch recording from an MLI at the initiation of the motorization period (engagement of the gear at 7 s). (**D**) Individual (gray) and average (black) spike waveform of the MLI from (C). (**E**) Wheel speed (violet), instantaneous firing rate (black) and spikes (grey, top) during extracts ($[4, 22]$ s) of consecutive recordings (first and last trial shown) from the same MLI. (**F**) Average waveforms and (**G**) cross-correlograms of an MLI from first (top row) and fifth trial (bottom row, same cell as in (E)). (**H**) Walking period firing rate over baseline period firing rate (paired Student's t-test: $t = 7.29$, $df = 63$, $p < 0.0001$); and (**I**) walking period CV over baseline period CV (paired Student's t-test: $t = -0.42$, $df = 63$, $p = 0.68$). Mean and STD are shown across trials for a given cell (panel (H),(I)). Cells recorded from the same animal in same color (see panel (H) where labels correspond to animal ID and total number of recorded cells per animal in parentheses). Top and right histograms show distribution of respective variable together with 25th (dotted), 50th (dashed) and 75th (dotted) percentiles. (**J**) Distribution of walking period correlation between firing rate and wheel speed ($N = 267$ for all recorded trials). Significant correlations ($p < 0.05$) shown in dark gray.

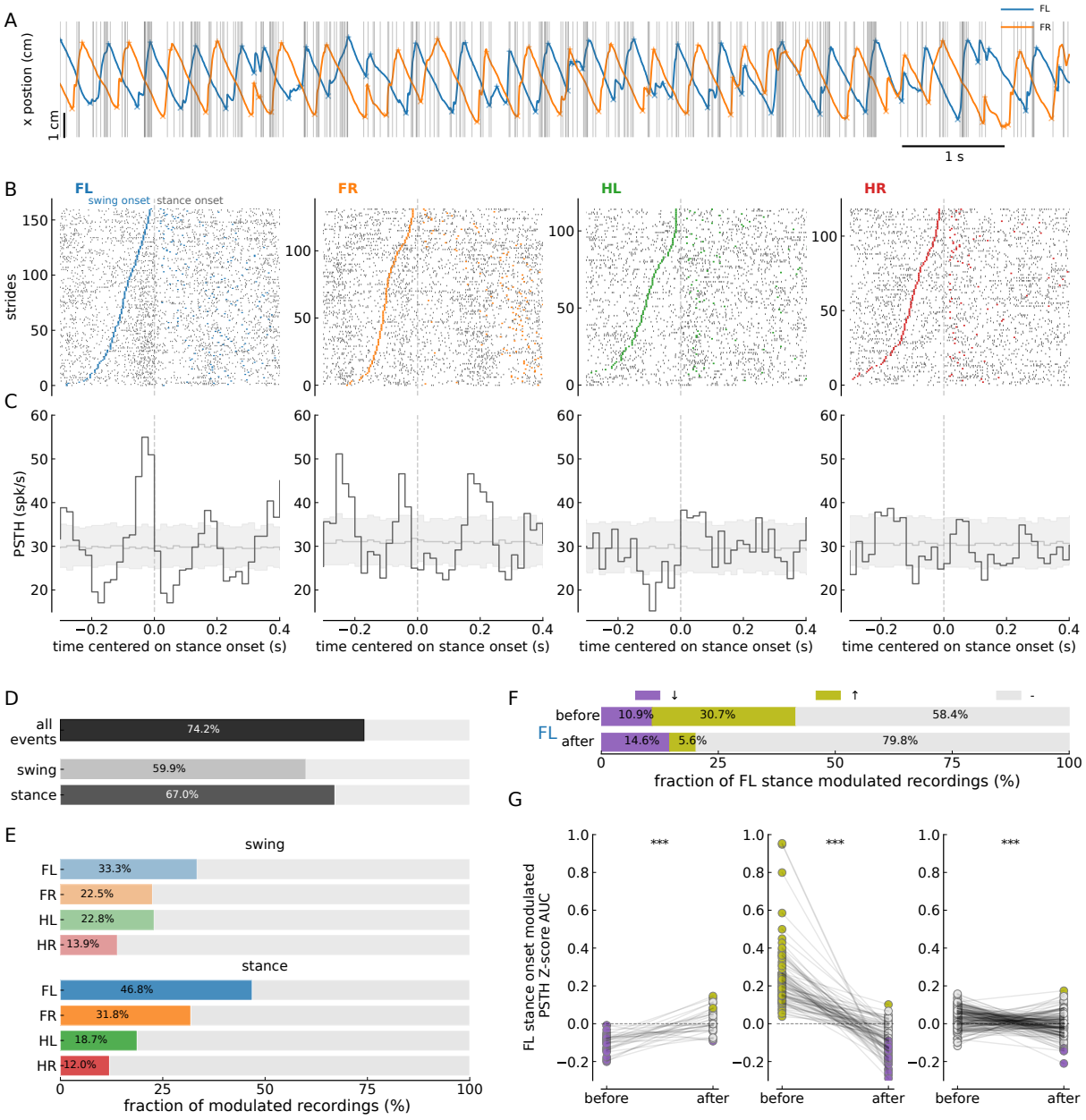

Figure 5: Stance onset-aligned MLI activity modulations. (**A**) Spiking activity of an example MLI (grey) and simultaneously recorded FL (blue) and FR paw (orange) x-positions during a sample period of a single trial. 'x' and '+' symbol represent swing onset and and offset, respectively. (**B**) Raster plots showing the occurrence of spikes aligned to stance onset (vertical gray dashed lines) during all strides of each paw (four columns for FL, FR, HL and HR from left), for an example recording of an MLI. Strides are sorted by swing duration. Colored ticks at negative times mark swing onset time for the swing ending at 0 s, and at positive times the swing onset for the subsequent swing. (**C**) Stance-onset aligned PSTHs corresponding to each paw's raster plot shown in (B). Pale gray lines and shaded area are mean and $[5, 95]$ percentile intervals of 300 stance-onset aligned PSTHs with shuffled spikes times (see Methods for details). (**D**) Bar plots showing the percentage of significantly modulated MLIs for all paws and all events (top bar), for swing- (middle), and stance-onset (bottom). (**E**) Paw resolved fraction of significantly modulated MLIs for swing-onset (top), and stance-onset events (bottom). (**F**) For the FL paw, the faction of significantly up ($\uparrow$), down ($\downarrow$), or not ($-$) modulated MLIs before- and after stance onset. The criterion for sig. modulation is two consecutive crossings of the $[5, 95]$ percentile interval of shuffled PSTHs during the 100 ms before or after stance onset. (**G**) The area under the z-scored PSTH curve (AUC) before and after FL stance-onset separated by before-down (left panel), before-up (middle) and before-not (right) modulated cells. The AUC before and after stance-onset of the same cells are connected with gray lines (paired Student's t-test; $***p < 0.001$ before vs after). All results is in this figure are based on individual recordings.

aligned activity (Becker and Person, 2019) and a signature of this could be present upstream in MLIs during the LocoReach task where paw forward movements resemble skilled reaches. To investigate this possibility, we explored peristimulus time histograms aligned to the extracted transition times from stance to swing and vice versa, called swing- and stance onset.

Strikingly, visual inspection of spike times aligned with the paw positions of an example recording revealed a preferred occurrence of spike discharges right before the peak x-position in many instances (example trace in Fig. 5A). This was true in particular for the FL paw and to a lesser extent for the FR paw. The peak x-position of the paws corresponds to the most forward position during the step cycle, that is, the end of the swing phase (steep upward spokes in Fig. 5A) and the beginning of the stance (slower downward strokes in Fig. 5A).

Across stride cycles, FL paw stance-onset alignment revealed a consistent peak activation during the end of the swing phase and a sharp drop in activity at the beginning of the stance phase for this example cell (left panels Fig. 5B,C). FR and HL stance-onset modulations were less pronounced in amplitude and no significant change was observed for the HR paw for the example recording (Fig. 5B,C). For the same recording, spikes were not aligned to stance onset (Fig. A.3A).

We quantified this effect in all MLIs and found that a large majority of cells (74.2 %) show significant firing rate modulations around the step cycle transitions of all four paws, with 59.9 % showing significant changes around swing-onset and 67 % around stance-onset (Fig. 5D). The FL paw stance-onset was the paw specific event which was accompanied most frequently by significant activity changes, *i.e.*, in almost half of the recordings (46.8 %; Fig. 5E) and possibly due to the predominantly ipsilateral control control of movement by the cerebellum (Darmohray et al., 2019). Fewer cells exhibited modulations around FR stance-onset (31.8 %), and swing-onset modulations were less common than stance-onset modulations for both paws (FL swing-onset: 33.5 %, FR swing-onset: 22.5). Firing rate changes around hind paw transitions were observed but less frequent than with the front paws (Fig. 5E).

Remarkably, the observed firing rate changes at step cycle events were not temporally symmetric around swing- or stance-onset but exhibited a sharp transition right at the onset time. To quantify this shape, we separated recordings according to significant increases (30.7 %), decreases (10.9 %) or no change (58.4 %) 100 ms before FL stance-onset (Fig. 5F) and swing-onset (Fig. A.3 C). When comparing activity dynamics before and after the onset event, the firing rate modulation changed significantly in each of the categories, and flipped sign in most cases (Fig. 5G, Fig. A.3D; quantified as area under the curve of z-scored PSTHs, analysis window 100 ms, see Methods for details).

The anticipatory activity modulation before the end of the stance and swing points to an event-specific role for many MLIs in lobulus simplex. Firing rate modulations occurred more frequently for stance- compared to swing-onset and for the front paws rather than the hind paws (Fig. 5E). Further indication that the observed activity pattern plays a role for the transitions comes from the fact that firing rate modulations before swing- or stance-onset were accompanied by a change in sign right at the beginning of the subsequent phase, *e.g.*, firing rate increases before stance-onset were accompanied by a firing rate decrease precisely timed to stance-onset and vice versa for rate decreases before stance-onset. In summary, we here revealed MLI firing rate modulations linked to events in the step cycle with the highest demands on motor control suggestive of a cerebellar implication for motor output precision and coordination.

Firing rate modulations are amplified for longer swings

Firing rate modulations linked to specific points in the step cycle could contribute to swing preparation and swing endpoint precision. We showed in Fig. 2 that single paw kinetics and precision as well as inter-paw coordination change over learning. In light of those results, we wondered whether firing rate modulations could be related to variations in swing-specific behavioral variables. We tested this by examining PSTHs across steps and trials for the same MLI, and compared the electrophysiological response with behavior since learning occurred across trials (Fig. 2).

The shape of the PSTH around swing-stance events was remarkably similar across trials for any given cell (Fig. 6A,B for example cells; A.4A). This shows that identical, event-related firing rate modulations are consistently evoked by specific swing-stance transitions. Intriguingly, rate modulations increased significantly when comparing first and last trials of swing- and stance onset modulated cells (FL: Fig. 6E,F; FR: Fig. A.4D,E). In other words, if significant firing rate changes existed around swing-stance transitions, their shape was preserved- and the amplitude of these modulations increased across trials. Overall, a majority of MLIs (70.3 %) showed significant rate modulations in at least one of the recorded trials at FL stance onset, and 59.4 % modulations at swing onset (Fig. 6C,D).

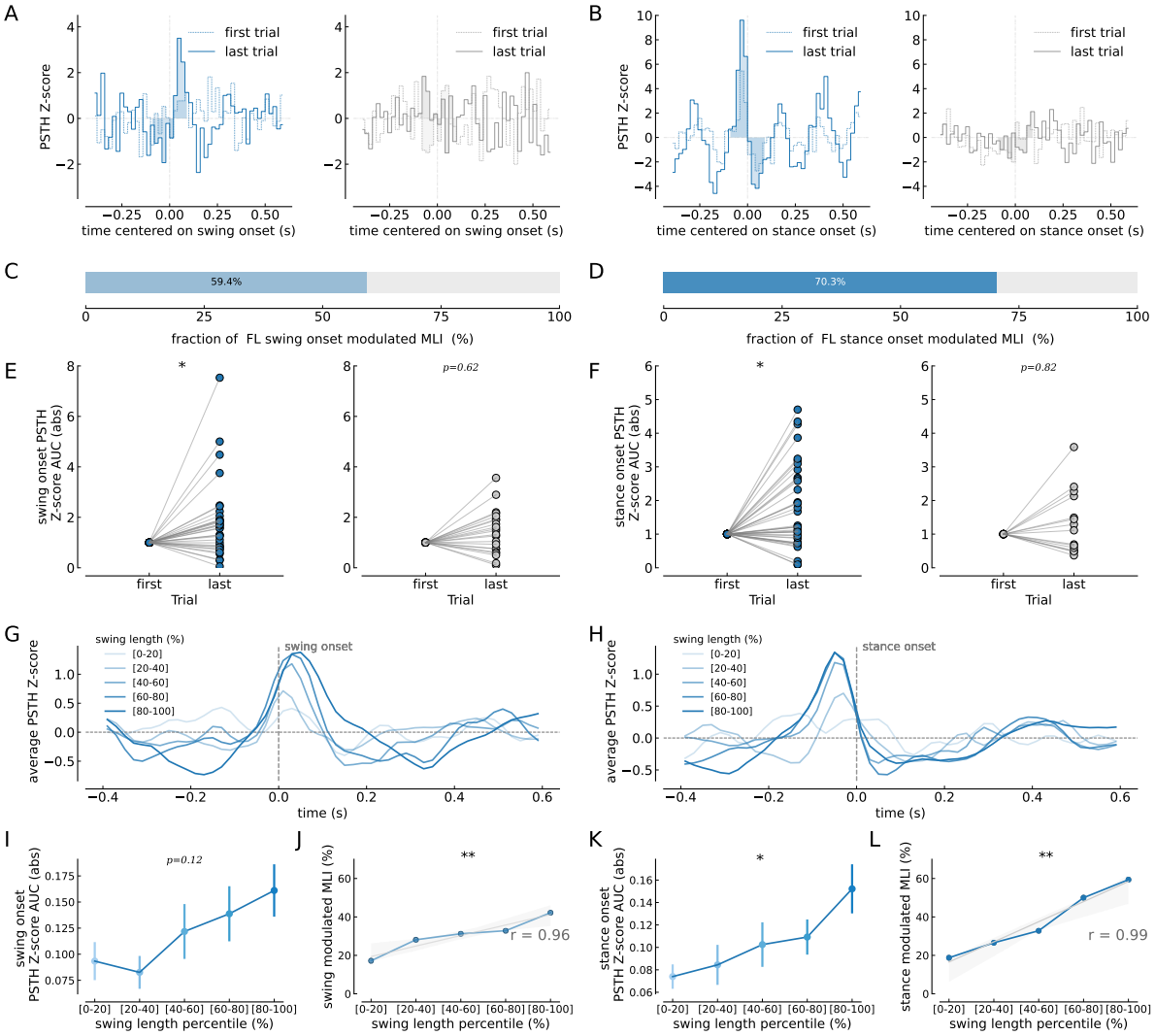

Figure 6: Across-trial FL paw swing- and stance onset-aligned MLI activity correlates with swing length. (**A**) Normalized FL swing onset-aligned PSTHs of an significantly modulated (left) and non-modulated (rigth) example MLI around swing onset. The z-scored PSTH for first (dashed/light line) and last trials (full line) are shown and the area under curve (AUC) is shown as shade region (analysis window $[-100, 100]$). (**B**) Same as (A) but for a modulated and non-modulated cell around FL stance onset. (**C, D**) Fraction of MLIs with at least one or more trials with significant modulations around FL swing (C) and stance (D) onset. (**E,F**) The area under the z-scored PSTH curve (AUC) around FL swing onset (E) and FL stance onset (F) is shown for the last trial relative to the first trial of modulated (left panel) and non-modulated (right panel) cells (analysis window $[-100, 100]$; paired Student's t-test, p-values reported in the panels). (**G**) Average FL stance onset-aligned, z-scored PSTH of significantly modulated MLIs for increasing ranges of swing length percentiles. (**H**) Same as (G) but for cells modulated around stance onset (**I,K**) AUC for swing (I, one-way ANOVA, $F = 1.868$, $p = 0.122$) and stance onset (K, one-way ANOVA, $F = 2.501$, $p = 0.046$) of cells modulated for a given range of swing length percentile, (**J,L**) Fraction of swing onset (J) and stance onset (L) modulated MLIs for ranges of swing length percentiles (Linear regression analysis, correlation coefficient r, and the significance of the regression p are reported in the panels). Significance is marked according to $*p < 0.05$, $**p < 0.01$, $***p < 0.001$.

We next asked whether the event-related firing rate modulations are linked to changes in behavioral parameters. Across trials, mice perform longer steps (Fig. 2B) and firing rate modulations around FL and FR swing- and stance onset increase in magnitude, as shown above (Fig. 6E,F). When combined, we found that activity changes at stance onset are significantly correlated with swing length (Fig. 6K). : the longer the length of the FL swing, the larger the modulation of activity around stance onset (Fig. 6H,K). Furthermore, the longer the FL swing the larger the fraction of cells that are significantly modulated around swing as well as stance onset (for FL: Fig. 6J,L; only for swing onset for FR: Fig. A.4G,I). We note that this difference in modulation occurs for strides within one session depending on their step length (swing length percentile based analysis of FL: Fig. 6I-L, see methods for details). In contrast, neither the activity modulation magnitude nor the fraction of modulated cells depended on the swing duration across trials (Fig. A.5C-F).

In summary, we found that longer swings imply stronger firing rate modulations and a larger fraction of modulated cells. On the other hand, swing duration is not correlated with firing rate modulations, consistent with the fact that long lasting steps are not far-reaching steps, *i.e.*, swing length and -duration are not correlated (Fig. 2I). As further reaches imply higher demands on swing endpoint control, a correlation of firing rate and swing length could suggest a role of MLI activity for swing endpoint precision.

Single MLIs get more entrained during learning and encode step cycle events of multiple paws

By analyizing PSTHs of MLIs, we revealed firing rate modulations which occurred at swing-stance (and stance-swing) transitions of specific paws. However, paw movements are periodic and coordinated between different limbs, which could impede a clear attribution of MLI activity modulations to single events. Moreover, as locomotor variables change over the course of a session, it is difficult to discern direct effects of learning on MLI activity from indirect effects, mediated by changes in locomotor parameters (*e.g.* swing length). We therefore devised a multi-step linear regression approach in order to uniquely attribute neural activity changes to single paw events, and to study the dependence of event-related responses on behavioral variables (such as swing length), as well as on learning over trials and across sessions.

We designed a general linear model (GLM) that took into account the discrete transition from stance to swing and vice versa for all four paws to explain single-cell firing rates in MLIs. A sequential L2-L1 regularized regression procedure allowed us to estimate the shape of event kernels, centered around behavioral events, and to add a sparsity bias so that a minimal set of behavioral variables impacts firing rates for each cell (Fig. 7C, see Methods for details, Musall et al., 2019). The resulting weighted event kernels captured the characteristic shape of firing rate modulations observed in the PSTH analysis, while controlling for spurious contributions emanating from time-lagged inter-paw correlations (Fig. 7D). As before, event kernels point to firing rate increases and decreases before and after swing-stance transitions, often with a sharp transition at the event time (see Fig. 7E for example kernel shapes).

We determined the contribution of specific events to single-cell firing rates by measuring the cross-validated R^2 of single-variable models (Musall et al., 2019; see Methods). Most cells responded to stance- (33/64) and swing (22/64) onsets of the FL paw, with fewer responsive to swing/stance events for the FR- or hind paws (Fig. 7F). This finding confirms results from the PSTH analyses, despite the sparsity constraint of the GLM. In support of specific event encoding of MLIs, adding continuous variables such as paw position, paw and wheel speed to the regression does not substantially increase the cross-validated R^2 (Fig. A.6D).

We next asked whether learning over sessions was related to stronger encoding of single-paw events. We divided sessions into early ($N = 34$) and late learning sessions ($N = 30$) for each mouse and asked whether single cells would show increased encoding of transition events. Given that a more coordinated gait late in learning (Fig. 2G,H) might spuriously lead to an increased number of significant events per cell, we measured the unique contribution of an event per session as the difference in R^2 between the full model and a model without the respective event regressor (Fig. A.6C). Even after this control, we found a significant increase in swing- and stance-encoding in cerebellar MLIs over sessions, especially for the front paws (Fig. 7G). Interestingly, we also observed that a fraction of cells were uniquely modulated by more than one paw (Fig. 7I). This fraction of mixed selective cells increased over sessions (Fig. 7J).

Finally, we investigated the fractional contribution of each of the discrete behavioral events to the overall explainable cross-validated variability in firing rate. Not surprisingly, removing the preferred event regressor from the linear model most strongly impacted the explained variance (Fig. 7H; $\Delta R^2/R^2_{tot} = 0.30$ $[0.20, 0.30, 0.36]$, mean, [25, 50 and 75 percentile]). In line with mixed contributions of several paws,

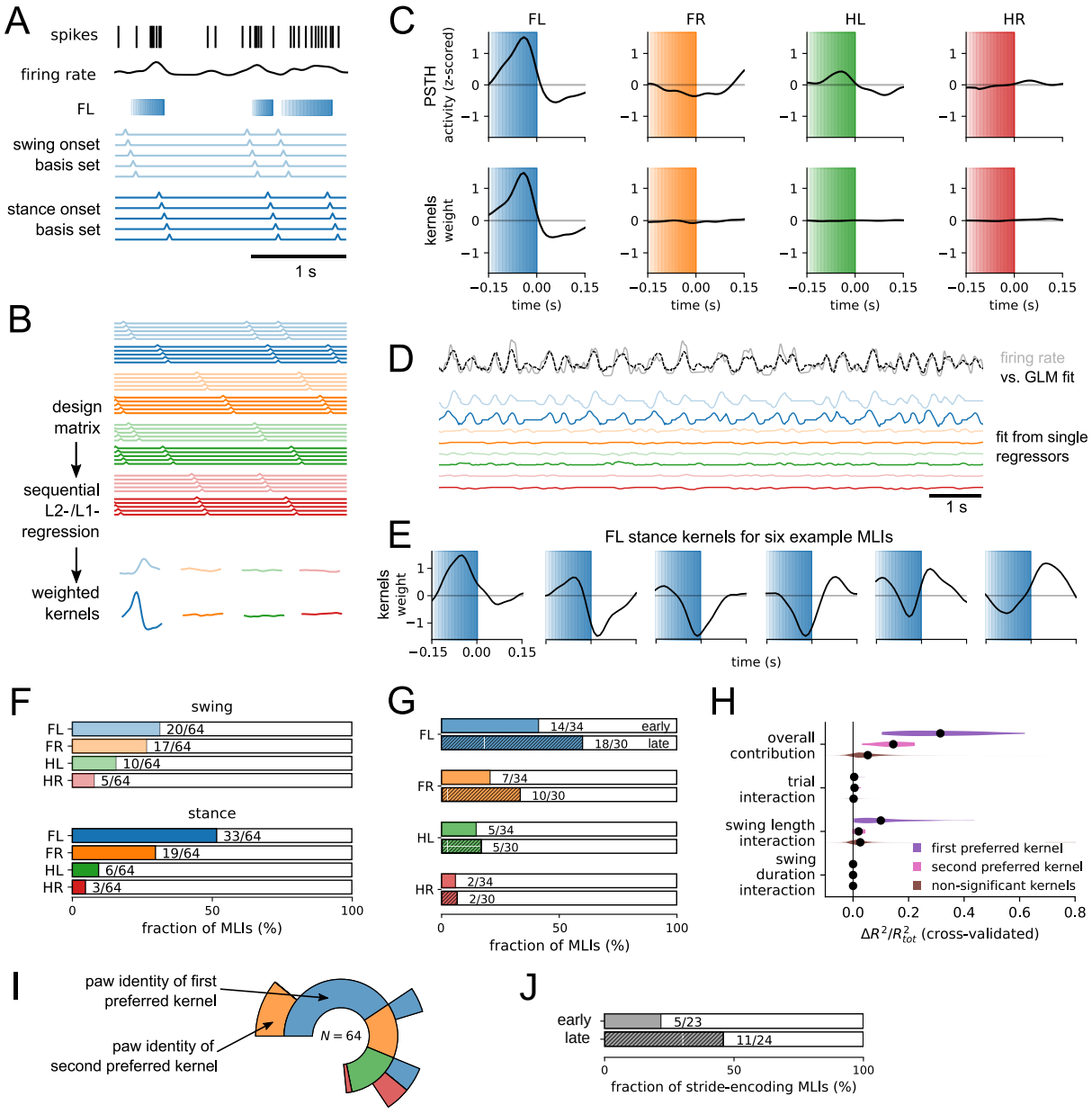

Figure 7: GLM analysis disentangles unique contributions of correlated behavioral events. (**A, B**) Schematic of the two-step GLM analysis of the instantaneous firing rate (black trace). Single-paw swings (graded bars) are encoded as a basis set of time-shifted binary event regressors centered at swing (pale traces) and stance onset (dark traces) (A). Swing- and stance onset basis sets for all four paws form the design matrix for a first, L2-regularized regression yielding event kernels (B) (Musall et al., 2019). Estimated kernels are then convolved with 8 binary event regressors (swing/stance for 4 paws) to form a new design matrix which also includes interaction terms. A second, L1-regularized regression step then provides a sparse representation of the behavioral events impacting firing rate. (**C**) Comparison of the paw specific PSTHs from z-scored firing rates (upper row; see Fig. 5) with the weighted event kernels from the two-step GLM (lower row) for an example cell. (**D**) Snippet from a linear regression example (10 s). Instantaneous firing rate (gray) and fitted firing rate (black) using 8 event regressors and their weighted contributions (colored traces). Paw and event colors as before. (**E**) Example kernels for the FL stance onset event obtained with the two step regression. (**F**) Fraction of cells with significant single-variable R^2 for different event types and paws. (**G**) Fraction of cells with significant difference in R^2 (pooling swing and stance regressors) in early (upper, solid bars) and late (lower, striped bars) sessions. (**H**) Unique contribution of different regressors (difference in R^2) to overall explained variance (R^2_{tot}). Purple, overall and interaction terms for first preferred event regressor (determined by absolute weight); pink, second preferred regressor; brown, non-significant event regressors. (**I**) Inner circle: Fraction of cells with at least one significant event regressor (swing or stance, difference in R^2), color-coded by paw identity. Outer circle, fraction of cells with a significant second event regressor. (**J**) Fraction of mixed selective cells (relative to cells with at least one significant event regressor), in early (upper) vs. late sessions (lower, striped bar).

removing the second preferred event still reduced explanatory power substantially $\Delta R^2/R^2_{tot} = 0.15$ $[0.11, 0.14, 0.18]$). Using the same approach, we also sought to confirm the differential influence of swing length, swing duration, and trial progression within a session on the strength of event-related responses in MLIs. To this end, we fitted GLMs that contained interaction terms of event regressors with trial numbers, swing length, and swing durations (adding a total of 24 interaction regressors). These extended models accounted for increases or decreases in event-related responses due to learning and behavioral parameters. We found that MLI event-responses were modulated by swing-length ($\Delta R^2/R^2_{tot} = 0.07$ $[0.03, 0.050.07]$). In contrast, de- or increases in MLI event responses over trials or in relation to swing duration were not significant (Fig. 7H). In other words, progressively longer steps over trials alone explain the increase in modulations in MLI activity (Fig. 7H).

Together, our linear regression analysis demonstrates that most MLIs respond to paw swing- or stance-related events, in accordance with the PSTH analyses. We show that MLIs in left simplex are most responsive to FL stances. Yet, several cells also encode other paw events, and in some cases, cells encode multiple paws at the same time. Over adaptation, we found an increased engagement of MLIs in task execution and an increase in mixed-selective cells. Changes in kernel weights across trials can be explained by taking into account the increase in swing length. In summary, the newly devised two-step GLM enabled us to capture variations in event-related responses stemming from behavioral factors and learning, singling out swing length as a central variable controlling how strongly swing-stance transition events influence firing rates.

Discussion

To study the role of molecular layer interneurons of the cerebellar lobulus simplex in movement precision and locomotor learning, we developed a forced locomotion paradigm of mice walking on a treadmill with rungs allowing to combine detailed analysis of paw movement kinematics with neural activity measurements, called LocoReach. We found that mice are adapting to the wheel speed and the rung distance by improving their locomotor performance over sessions, *e.g.*, they perform longer and more precise steps. We showed for the first time that MLI activity is related to specific events in the gait cycle – transitions from swing to stance and vice versa – most prevalent for the FL paw, located ipsilateral to the recording site, followed by the FR paw and less often observed for the hind paws. Using PSTH and GLM analysis, we demonstrated that activity modulations correlate with step length. Using closed-loop optogenetic perturbations during front left swing phases, we support this finding by showing that inhibiting lobule simplex output curtails swings in a paw-specific fashion. Later during learning, more cells encode paw events and more cells exhibit mixed-selectivity for more than one paw.

Several of our findings reproduce previous results from related tasks. Mice adapt their stepping patterns on runged surfaces by increasing their step length and reducing the number of miss steps (Fig. 2; Vinueza Veloz et al., 2015). Engagement in locomotion on the runged treadmill elicits a significant increase in MLI activity (Fig. 4H) similar to what has been reported for walking on flat surfaces (Jelitai et al., 2016; Ozden et al., 2012) or walking on a slope (Lyu et al., 2022). In line with the fact that cerebellar control of movement is predominantly ipsilateral (Darmohray et al., 2019; Heffley et al., 2018; Lee et al., 2015), we found that most cells in the left simplex were tuned to ipsilateral front left paw events, also the hind left paw events were more often observed than hind right events (Figs. 5E and 7F,G). Step-related discharges have been reported to be widely distributed in the cerebellar cortex and nuclei during visually-guided ladder walking of cats, including in the intermediate cerebellum, which is the focus of this study, and the interposed nucleus (Armstrong and Marple-Horvat, 1996).

Other results are novel and open a new perspective of MLI function in locomotor control. Rather than being linked to continuous kinematic variables of limb movements in PCs (Edgley and Lidierth, 1988; Hewitt et al., 2015; Hewitt et al., 2011; Pasalar et al., 2006) or lick rate in MLIs (Gaffield and Christie, 2017), we showed that MLI activity encodes specific behavioral events suggesting a punctual rather than a continuous task engagement. And MLI engagement occurred at points with heightened demands on motor output control, *i.e.*, the swing start and end points. Beyond ipsilateral movement control, a large number of MLIs responded to contralateral FR and HR events (Figs. 5E and A.4), or showed mixed-selectivity for multiple paws from opposite sides of the body (Fig. 7I). The mixed selectivity for multiple limb movements could allow MLIs to integrate information across cerebellar microzones to coordinate multi-joint dynamics. Modulation of PC activity occurs in relation to the step cycle for walking on flat surfaces (Armstrong and Edgley, 1984; Armstrong et al., 1988; Edgley and Lidierth, 1988; Sauerbrei et al., 2015) or on a ladder (Armstrong and Marple-Horvat, 1996). However, individual cells vary greatly in the phasing of their discharge relative to the step cycle (Armstrong and Marple-Horvat, 1996;

Sauerbrei et al., 2015), similarly observed for PCs during skilled reaching (Calame et al., 2023). During walking, population and not single cell activity is at its highest level during the ipsilateral forelimb swing and around the period around footfall (Armstrong and Marple-Horvat, 1996). In contrast, the activity modulation reported here occurs surprisingly consistent across the recorded MLI population linked to the transition events from swing to stance and vice versa, which suggests a more homogeneous MLI population response. This intriguing homogeneity may be attributed to enhanced synchrony within the MLI network, possibly facilitated by gap junctions (Kim et al., 2014).

Purkinje cells and neurons in the interposed nucleus are modulated during and near the endpoint in a reaching task and this activity is necessary to convey kinematic information as well as to slow the limb near endpoint (Becker and Person, 2019; Calame et al., 2023). The encoding of swing-stance transitions by MLIs in lobulus simplex that we observed could provide a potential source for this endpoint alignment in the cerebellar nuclei. The increased MLI activity precisely timed around stance onset could convey swing endpoint information downstream via graded inhibition of Purkinje cell output. In turn, disinhibition of the cerebellar nuclei near swing termination would then enable encoding of reach endpoint kinematics to adjust endpoint precision. This idea is in line with our finding that longer steps elicit larger activity modulations due to their higher need for control. Step-length modulated and stance onset locked MLI firing patterns could be an essential part of the cerebellar cortex circuitry that enables encoding of reach-related kinematics in the deep nuclei.

The reduction in ipsilateral swing length induced by closed-loop optogenetic interference provides causal evidence for the role of lobule simplex in controlling paw movements during locomotion. This effect implies that silencing cerebellar cortex activity prematurely terminates the forward progression of the limb. The observed reduction in swing length in the current study aligns conceptually with the scaling of limb kinematics with activity in the anterior interposed nucleus (IntA, Becker and Person, 2019) which is the major target of lobulus simplex PCs. Activating IntA neurons curtails reaches (Becker and Person, 2019), consistent with our observation that the inhibition of PCs performed in this study (which in turn disinhibts IntA neurons) leads to shorter swings. In both locomotion and reaching contexts, the cerebellar lobule simplex emerges as a key player in modulating the phase and paw positioning, thereby orchestrating precise and coordinated movements.

Despite altered locomotor kinetics under both muscimol and optogenetic interference, the fraction of miss-steps remains surprisingly consistent between perturbed and control animals. This observation may unveil underlying compensatory strategies that mitigate the impact of cerebellar inhibition on task performance, *i.e.*, the animal might recede to smaller steps of reduced demand on position control when perturbed and thereby preserve the fraction of paw end-point misplacements. The disruption in inter-limb coordination might be a direct result of perturbed FL movements, or point to a broader role of the lobule simplex in regulating multi-limb movement patterns. The latter together with our finding of mixed selective cells for multiple paws would provide evidence that the lobule simplex is involved in the online computation and control of limb dynamics critical for coordinating multi-limb movements during locomotion. An important next step will be to decipher cell type specific contributions to the observed locomotor effects.

The predictable effect of the closed-loop perturbation, always occurring at a fixed delay during the swing phase, got compensated and no difference in locomotor parameters between perturbed and control animals was apparent after a few sessions (Fig. 3D,F). This is reminiscent of the adaptation reported upon repeated mossy fiber stimulation during reaches (Calame et al., 2023), and fits into the framework that consistent and predictable consequences of behavior are learned and compensated by the cerebellar circuitry (Sawtell, 2017). Further work is required to decipher the mechanism of the compensation reported here, and which is typically associated with plasticity at the parallel fiber - PC synapse (Sawtell, 2017).

Variations in step length dynamically impose modulations of the firing rate transients reported here. These changes in swing-stance transition triggered MLI activity are most likely inherited from changes in granule cell activation and mediated by parallel fibers, as the sensorimotor context of a task is thought to be encoded by granule cell activity (Albus, 1971; Marr, 1969). Depending on the relative weight of direct excitatory inputs to PCs from parallel fibers and inhibitory input through the parallel fiber - MLI pathway to PCs, MLI-mediated inhibition can allow to independently regulate both the baseline activity and the magnitude and direction of firing rate modulation in Purkinje cells during swing-stance transitions. Whether the change in the fraction of modulated cells across learning (sessions) is due to plasticity at the parallel fiber – MLI synapse (Mapelli et al., 2015) remains to be determined.

While classic models have focused on the granule cell to Purkinje cell pathway as the key site of sensorimotor prediction (Sawtell, 2017), the MLI encoding of limb events across locomotor learning

could point to a more active role for cerebellar interneurons. This possibility is further supported by the fact that MLI firing rate modulations occured most frequently at stance onset when the mouse terminates a reaching movement for a chosen rung, as recent work has shown that the cerebellar nuclear neurons targeted by Purkinje cells in the simplex bidirectionally encode endpoint velocity in a reaching task (Becker and Person, 2019). Future explorations including recordings of cerebellar input - from mossy fiber, granule cells - and output signals - from Purkinje cells - of the cerebellar cortex during the LocoReach task will further clarify how cerebellar circuit processing enables precise motor coordination.

An open question is whether the observed encoding patterns are consistent across MLI subtypes, or differ between stellate and basket cells or MLI2 (Lackey et al., 2023). Our loose cell-attached recordings may have over-sampled stellate cells located superficially. Future work could examine encoding specificity of MLIs leveraging genetic access to subclasses of MLIs.

Locomotion was imposed by the treadmill motorization rather than self-initiated. Although, we assume that cerebellar processing of the reaching component of the task bears no difference to free walking on runged surfaces, MLI encoding could differ during spontaneous, voluntary or goal-directed locomotion.

The newly developed LocoReach task allows for the simultaneous study of high precision motor output and neural activity. Here, we focus on recording spiking activity of single MLIs. The locomotor task is continuous but we find that MLI activity is linked to specific instances in the stepping cycle, *i.e.*, situations with heightened demands on the precision of locomotor output. Such intermittent engagement across the population has not been reported before and proposes a new role of MLIs in locomotion. This discovery promises new exciting avenues for understanding cerebellar and cerebral function during complex locomotion using LocoReach.

Methods

Experimental procedures complied with animal care guidelines of the Université Paris Cité. Experimental procedures were approved by the French Ministry of Higher Education, Research and Innovation (APAFIS#11158-2017041316199 v8) in agreement with the European Directive 86/609/EEC and by the ethical committee of the Université Paris Cité.

LocoReach setup

The LocoReach setup allows the study of the fine details of performance, motor coordination, and learning during skilled locomotion on a treadmill with rungs. The custom treadmill comprised 48 rungs (3 mm diameter, 80 mm long) equally spaced every 1.65 cm (Fig. 1A; outer circumference 80.4 cm) and was 3D printed in semi-transparent material (WaterShed XC 11122) through Stereolithography (Protolabs Euro Services Limited). The half-open treadmill design allowed to place a custom laser-cut acrylic mirror at a $\sim 45°$ angle in the wheel, under the animal. The wheel rotated freely and allowed for self-paced locomotion. For motorization, a servo motor (Futaba S3004, servo 1 in Fig. 1A) moved into a gear and another continuous servo motor (Parallax Continuous Rotation Servo, #900-00008; servo 2 in Fig. 1A) imposed a constant baseline speed of 7.49 cm/s, and 5.8 cm/s in the musciol/saline experiments. On flat surfaces for comparison, mice exhibit the slowest gait pattern 'walk' - *i.e.* at least three paws simultaneously on the ground - with average speeds of 9 ± 5 cm/s ($\pm$ SD) but can reach maximal moving speeds of up to 100 cm/s (Bellardita and Kiehn, 2015; Machado et al., 2015). The rotation of the wheel was recorded with a rotary encoder (CUI Devices, AMT112S-V, resolution: 2048 pulses per rotation), digitized at 40 kHz with a standard DAQ acquisition board (National Instruments, PCIe 6323) and acquired with ACQ4 (Campagnola et al., 2014). Mice were illuminated with infra-red light (a ring of 10 LEDs of 940 nm - Thorlabs LED940E - located around the objective of the camera), videographed at 200 frames/s (camera: Dalsa Genie Nano, NANO-M800-NIR; objective: Fujinon DF6HA-1B; positioned 22 cm from the center of the treadmill) and videos were acquired with ACQ4. An array of four flashing infra-red LEDs (Thorlabs LED940E) was placed to appear in the upper right corner of the behavioral videos (Fig. 1B) and used to synchronize video frames with the electrophysiological- and rotary encoder recordings. Transparent acrylic side walls restricted the animal's position to the center of the runged surface of the treadmill (Fig. 1A).

Animals

For the electrophysiological recordings, we used transgenic animals (five males and six females, aged 1-3 months) issued from a cross of mice carrying the GCaMP6f transgene in the Igs7 locus (Ai93(TITL-

GCaMP6f)-D; Jackson laboratory stock # 024107) and B6 PV-Cre mice (Jackson laboratory stock # 017320). For the muscimol infusion experiments, we used B6 PV-Cre mice (seven males and eight females, aged 1-3 months). All animals lived under inverted day/night cycle with ad libitum access to food and water in enriched environments.

Chronic window with access port and head-plate surgery

Mice were prepared for electrophysiological recordings during locomotion by implanting a chronic window with silicone access port (Roome and Kuhn, 2014) and fixing a head post. Before surgery (10–15 min), mice were injected with buprenorphine (0.35 mg/kg intraperitoneal) for pain reduction. Lidocaine was used as a local anesthetic before skin opening. Surgeries were performed under isoflurane (1.5–2.0 % by volume in air) to maintain a surgical plane of anesthesia as determined by non-responsiveness to toe pinch. Eye ointment was applied under anesthesia at the start of surgery. Animals were held in a stereotaxic apparatus using ear and nose bars to stabilize the head. Body temperature was set with a heating pad and controller at 37 °C using biofeedback from a rectal thermocouple.

For the surgical procedure, the area of the head over the intermediate cerebellum was first shaved and the underlying skin was treated repeatedly with ethanol (70 %) and Vetedine solution (Centravet) in alternation. The skin above the skull was removed and the opening of the periosteum as well as any membranous tissue were cleaned. Once the skull was dry, a cranial window was carefully drilled using a handheld high-speed micromotor drill (Foredom, FST burr #19007 − 05 with 0.5 mm tip diameter). The center of the craniotomoy was located −6 mm AP and 2 mm ML targeting the left lobulus simplex. Skull removal was performed under application of an ACSF solution to minimize the risk of damaging the dura overlying the brain. After skull removal, the ACSF solution was used to clean any debris from the brain surface and to maintain the brain moist providing an interface to the chronic window. A chronic window was fabricated from a cover glass (#1, thickness 150 μm) laser cut to a small oval shape (3 mm x 2.6 mm) to better fit the cranial opening, and to feature a central hole of $\sim$ 500 μm diameter for electrode entry. Prior to surgery, the cut hole was sealed with Silgard 184 (Roome and Kuhn, 2014). The window was placed over the cerebellar lobulus simplex and kept in direct contact with the brain by lowering the window with the help of a needle mounted in the stereotaxic setup. The chronic window was fixed in place with dental cement (Super-Bond C & B). After setting of the dental cement, the bone surrounding the craniotomy was thinned with the micromotor drill to allow for better access with the 20x objective and recording electrode. Then a custom-made stainless steel head post with a central opening for the craniotomy was cemented in place with dental cement (Super-Bond C & B). The chronic window was covered with silicone for protective purposes after surgery. Mice were carefully monitored during surgical recovery, with all animals showing normal behavior including the absence of motor deficits. Mice were allowed to recover at least 2 days before proceeding to the locomotion and electrophysiological recording experiments with ad libitum access to food and water.

Stereotaxic guide cannula implanation and muscimol injection

To test the causal implication of the lobulus simplex in LocoReach motor learning, we reversibly and repeatedly performed inactivations by infusion of the $GABA_A$ agonist muscimol. For that purpose, we unilaterally implanted a guide cannula. Animals followed the same preparatory steps as described above for the chronic window surgery until the cleaning of the skull in the stereotaxic setup. To target the left lobulus simplex, a cranial opening ($\sim$ 700 μm diamter) was carefully drilled centered at AP −6 mm, ML 2 mm. Next, a cannula (26 gauge, 2.5 mm shaft, Plastics One, C315GS-4) was placed in a 3D-printed custom holder and lowered to the target location of 200 μm below the brain surface. Dental cement (Super-Bond C & B) was applied around the implant and a custom-made stainless steel head post with a central opening for the cannula was cemented in place. The guide cannula was sealed by threading a dummy cannula with aluminium cap. Mice were allowed to recover at least 2 days before proceeding to the locomotion and inactivation experiments with ad libitum access to food and water.

Prior to the adapation protocol, saline ($N = 7$) or muscimol ($N = 8$, conjugate of muscimol and the Bodipy TMR-X fluorophore, Invitrogen^{TM}; purchased from Thermo Fisher Scientific, reference M23400) disolved in PBS (ph 7.4; 0.5 μg/μl) was infused into the left lobulus simplex using an ultra-fine silica fiber needle (inner diameter 75 μm, outer dia. 150 μm; custom build by PHYMEP, Paris) connected to a 25 μl Hamilton syringe (Model 1702 RN SYR) mounted in a stereotaxic nanoliter pump (KD Scientific, Legato 130 syringe pump). Mice were placed under isolfurane induced anesthesia during perfusion. The tip of the internal cannula protruded 700 μm beyond the implanted guide cannula (*i.e.*, 900 μm total depth below simplex surface). The infusion rate (0.08 μl per min) was controlled by the syringe pump.

The total volume of each simplex infusion was 0.40 μl. The internal cannula was retracted 5 min after the infusion and the behavioral session started 30 min after the start of the infusion.

LocoReach learning protocol

Prior to locomotor sessions, mice were habituated to the LocoReach setup and the head-fixation (attachment of the surgically implanted head-post to a rigid fixture) on top of the treadmill. For habituation, the treadmill's surface was covered with a plastic mesh (square grid of 5 $\times$ 5 mm) allowing for easy grip. Head-fixation time was gradually increased during four habituation sessions spread over two days, and wheel motorization (same as described below during locomotor sessions) during head-fixation was introduced at the third habituation session.

Mice were positioned with the tip of the nose $\sim$ 5 mm above the spherical treadmill, and with an angle of $\sim 10^{\circ}$ between the tangent of the treadmill and the bottom of the lower jaw, a position which was inferred from inspecting free walking on the treadmill. One session consisted of multiple (typically 5, range: $1-8$) 1 min recording trials which were repeated every 2 – 4 min, *i.e.*, with rest periods of at least 1 min between trials. The speed and the duration of locomotion during the recordings were imposed in an attempt to minimize variations across recordings. The forced locomotion scheme was as follows: recordings started with a 6 s long period of baseline during which the mouse was able to freely walk on the treadmill. At 6 s, servo motor 1 moved the continuous rotation servo 2 in a gear attached to the axis of the treadmill (Fig. 1A). The continuous servo started to linearly accelerates (2.5 cm/s^2) the wheel at 7 s until the constant baseline speed of 7.49 cm/s was reached at 10 s. This rotation speed was kept constant for 42 s until 52 s at which point the motor linearly decelerated (-2.5 cm/s^2) until standstill at 55 s and then moved out the gear from the treadmill axis allowing for self-paced walking.

Stereotaxic injections, optical fiber implantation and close-loop optogenetic manipulation

For the optogenetic interference experiments, the animals underwent the same surgical procedures as outlined above for the chronic window implantation, up to the point of skull cleaning in the stereotaxic setup. A cranial window of $\sim$ 500 μm diameter was then carefully drilled using a handheld high-speed micromotor drill (Foredom, FST burr #19007 $-$ 05 with 0.5 mm tip diameter). The center of the craniotomoy was located -6 mm AP and 2 mm ML targeting the left lobulus simplex. Subsequently, PV-cre mice received unilateral injections in the left lobule simplex of 0.7 μl of pAAV-1-hSyn1-Flex-SIO-stGtACR2-FusionRed-dlox ($N = 5$, 2.0×10^{12} genome copies/mL; Addgene: 105677-AAV1), while another group of PV-cre mice received injections of pAAV-9/2-hSyn1-dlox-tdTomato-dlox-WPRE ($N = 3$, 6.1×10^{10} genome copies/ml; VVF Zurich: v663-1). These injections were administered through the craniotomy using a Hamilton syringe (Model 7001, Hamilton) at a rate of 0.1 μl/min, employing a glass capillary needle with a diameter ranging from 14 to 18 μm. The injection site was localized to the left lobulus simplex (coordinates: anterior-posterior -6 mm, medial-lateral 2 mm, dorsoventral 0.35 mm). Following each injection, the needle remained in situ for 5 minutes to mitigate backflow before being slowly retracted. Subsequent to the injection procedure, an optical fiber (core diameter 200 μm, numerical aperture 0.39, Thorlabs Inc.) affixed to a ferule (1.25 mm diameter) was implanted above the injection site (coordinates: anterior-posterior -6 mm, medial-lateral 2 mm, dorsoventral 0.325 mm) and secured to the skull using dental cement (Super-Bond C & B).

Real-time tracking of the position of the left forepaw was achieved using Bonsai during the behavioral experiments (Lopes et al., 2015). Using the animal video stream, a region of interest was placed to comprise the ensemble of FL positions during the task in Bonsai. Image of this ROI underwent multiple processing steps to extract the center of mass of the paw. Whenever the FL center of mass displacement across consecutive frames exceeded a threshold, which was adjusted to identify swing onset, the laser was triggered for 80 ms through a Bonsai-controlled Arduino. The delay between threshold crossing and trigger signal as well as the duration were adjusted to achieve laser activation during and at the end of the swing phase (Fig. 3A).

The behavioral task started four weeks following the virus injection. Before exposure to the LocoReach task, mice underwent the same habituation procedure as outlines above. The optical fiber was connected to the implanted ferule and the real-time extraction parameters (ROI of the front left paw) were adjusted in Bonsai prior to each locomotor session. Optical stimulation was administered using a laser (405 nm wavelength) coupled to a patch cord fiber (core diameter 500 μm, numerical aperture 0.5, Thorlabs), with an output intensity of 30 mW from the fiber tip.

Cell-attached recordings

We conducted cell-attached recordings of the electrical activity of MLIs in the left lobulus simplex of PV-cre/Ai93(TITL-GCaMP6f)-D mice during the acquisition of the LocoRung task. These mice expressed GCaMP6 in *sim*50 % of MLIs throughout the cerebellar cortex. We used long-shaft patch pipettes ($5 - 10$ MΩ resistance) loaded with Alexa 594 (50 μM) in ACSF (150 mM NaCl, 2.5 mM KCl, 1.5 mM $CaCl_2$, 1 mM $MgCl_2$, 10 mM Hepes, pH 7.3, $280 - 300$ mOsm), and performed two-photon microscopy-guided recordings of MLIs identified through their molecular layer localization and by GCaMP6 expression through a chronic window with a silicone access port that allowed for repeated electrode penetration over days (Figure 4A,B; details of the custom build 2-photon laser scanning setup can be found in Franconville et al., 2011). The current traces of the cell-attached recordings were recorded in voltage-clamp mode using a Axopatch 200B amplifier (Molecular Devices), digitized at 40 kHz (National Instruments, PCIe 6323), and acquired with ACQ4 (Campagnola et al., 2014). In some cases, we also performed blind recordings in which cells were identified through clustering based on the cell's electrophysiological signature as MLIs or PCs (Fig. Figure A.2, see below for details).

Raw electrophysiological traces were analyzed in P-sort to detect spikes of MLIs and simple as well as complex spikes for Purkinje cell recordings (Sedaghat-Nejad et al., 2021). Current traces were band-pass filtered (0.5 to 5 kHz) and spikes clustered using the build-in nonlinear dimensionality reduction in P-sort.

To further distinguish between MLIs and PCs, we used t-distributed stochastic neighbor embedding (t-SNE; parameters: n_components= 2, perplexity= 45, early_exaggeration= 18) clustering based on the average action potential waveform, the spike auto-correlogram, the firing rate, the trough-to-peak delay of the average spike waveform, the spike-count coefficient of variation for multiple bin sizes (0.05 s, 0.5 s, 1 s and 5 s), and the existence of complex spikes as binary variable (Fig. A.2). This method identified two separate clusters containing putative MLIs and PCs, respectively. All analysis in this study was performed on the MLI cluster. The MLI cluster contains 64 cells from a total of 11 mice, most with 5 trials per cell per recording session (Fig. A.2A inset). We discontinued recordings for a given mouse when it reached 10 recording sessions or when the chronic window quality decreased due to dura regrowth or tissue thickening. Cells with unstable spike signals (*e.g.*, complete disappearance of spikes for prolonged periods) during the 60 second trial period were excluded from the analysis.

Paw tracking and swing-stance fragmentation

The videos recorded during the locomotor sesions were analyzed using DeepLabCut (DLC; Mathis et al., 2018) to extract the x- and y-positions of front left (FL), front right (FR), hind left (HL) and hind right (HR) paws across individual frames in the bottom view of the animal (Fig. 1B,C). Multiple DLC relabelling and retraining iterations were performed to achieve a target error rate of < 0.0005 % per video, where errors were identified when paw displacement speed across successive frames exceeded > 60 pixels/s. Individual frames which exceeded this threshold were excluded from further analysis. Using the congruent paw- and wheel speed periods during stance and the known wheel speed at the surface of the treadmill, we transformed the paw speed extracted from the videos into cm/s, using the scaling factor 0.025 cm/pixel. A custom-written Python script was used to track the position of all rungs present in each video frame, based on the fixed and consistent spacing between the rungs. The relative difference between paw x-speed and wheel speed (speed difference > 10 cm/s for at least three consecutive frames), as well as the paw-to-rung distance (paw and mouse specific based on the histogram of paw-rung distances) were used to segregate the paw trajectories into swing and stance phases (Fig. 1D). Miss steps were extracted based on multimodal paw speed profiles during the swing face indicative of alternating deceleration and acceleration phases due to attempted rung approaches. That is, if the relative paw-speed (paw speed - wheel speed) dropped below 10 cm/s for at least three consecutive values (excluding the beginning and the end of the swing) or for at least three times, the swing was classified as a 'miss step'. These values were determined through visually inspection of the resulting step classification in the video recordings. Using extracted paw positions, paw speed, swing-stance phases, rung locations and miss steps, we computed the stride- and inter-paw coordination parameters shown in Fig. 2 and **??**.

PSTH analysis

Peristimulus time histograms were computed based on consecutive bins (bins size 20 ms) of spike times in the interval $[-300, 400]$ ms centered on all swing- or stance onsets of a recording, and normalized by the number of events and the bin size to yield average firing rate. Shuffled PSTHs are obtained through

jittering the original spike train by adding to each spike an independent Gaussian random variable of zero mean and $J = 500$ ms standrard deviation (STD), which eliminates correlations to behavior on time-scales $\ll J$. The mean shuffled PSTH, the 5th and 95th percentiles and the STD along the interval $[-300, 400]$ ms was computed from 300 shuffled PSTHs obtained with different random number seeds. Individual recordings were classified as significantly up/down modulated before or after an event, if the PSTH crossed the 95th/5th percentile of the shuffled PSTHs for at least two consecutive values in the 100 ms interval preceding or following stance- or swing onset. The z-scored PSTH was calculated using the shuffled PSTHs according to $PSTH_{\text{z-scored}} = (PSTH - \overline{PSTH_{\text{shuffle}}})/STD(PSTH_{\text{shuffle}})$. And the area under the curve (AUC) of the z-scored PSTH corresponds the integral of absolute values over the interval $[-100, 0]$ ms for before, $[0, 100]$ ms for after stance- or swing onset, and over $[-100, 100]$ ms for the combined AUC.

For the swing-length and swing-duration percentile-based analysis (Figs. 6, A.4, A.5), all swings of a given cell during one session of multiple trials where subdivided according to the percentile ranges $[0-20]$, $[20-40]$, $[40-60]$, $[60-80]$, $[80-100]$ of all swing lengths or durations. The z-scored PSTH was then calculated for swings falling withing a specific percentile range. The AUC and whether a cell in a given percentile range was modulated or not was evaluated as specified above.

Event kernels and linear models

To measure the influence of swing- and stance-onsets on MLI firing rates, we fitted L2- and L1-penalized linear models in Python, implemented in the package scikit-learn ("Ridge" and "Lasso", respectively). Firing rates were calculated from binned counts with a bin size of 10 ms. We detrended firing rates by subtracting smoothed signals (Gaussian filter with $\sigma = 300ms$) and subsequently smoothed rates using a Gaussian kernel ($\sigma = 20ms$). After selecting motorized periods, we z-scored and concatenated all recordings from the same cell.

Multistep linear regression was performed by first constructing the design matrix for event kernel estimation: For each limb and event type (swing vs. stance onset), we included a set of 31 time-shifted delta-function regressors that spanned the peri-event period from 150 ms before to 150 ms after each event, resulting in a $248(31 \times 2 \times 4) \times N_{timepoints}$ design matrix. Event kernels were obtained as the set of 31 L2-regularized weights for each limb and event.

For the sparsity-constrained second regression step, we normalized event kernels to have maximum absolute weights equal to 1. We then convolved kernels with the indicator function for the respective event, resulting in a $8 \times N_{timepoints}$ design matrix for 4 limbs and 2 event types. For analyses including interaction terms (event $\times$ trial number, event $\times$ step length, event $\times$ swing duration), we multiplied all 8 event regressors with the associated value, resulting in a $32 \times N_{timepoints}$ design matrix. In Fig. A.6D, we also included 17 continuous regressors (wheel velocity, x- and y-positions for each limb, and wheel-velocity corrected speed along x and y for each limb). We then estimated L1-regularized weights based on the new design matrix.

Cross-validation was performed to determine optimal L2- and L1-regularization hyperparameters. We first chunked time series into pieces of 90 ms. To decorrelate adjacent data points (which are correlated due to Gaussian smoothing), we removed the first and last 20 ms from each chunk of data. We then randomly assigned chunks to train and test set (80% vs. 20%). Optimal L1- and L2-parameters were determined based on the maximal model R^2 on test data. Cross-validated R^2 was also used to determine the significance of single regressors: For each event, we shuffled temporal chunks of 200 ms of the regressor of interest before performing the L2-regularized regression step. For interaction terms, we shuffled the respective modulating variable (trial number, step length, swing duration) after performing L2-, but before performing L1-regularized regression. To measure the unique contribution of a variable (ΔR^2), we calculated the difference in R^2 between the model where the variable of interest was shuffled vs. the R^2 on the full (unshuffled) model. Single-variable R^2 values were measured after shuffling all variables but the variable of interest (Musall et al., 2019). We repeated cross-validation 100 times on random train/test splits to calculate 95% confidence intervals for each measure. Variables were considered to have a significant effect if confidence intervals of single-variable R^2 or ΔR^2 were above zero (Figs. 7 and A.6).

Statistics

Statistical differences in locomotor parameters were analyzed using mixed linear models with session, trial, paw as fixed effects variables and animal as a random effect ($parameter = session + trial + paw + (1|animal)$). For lobule simplex inactivation experiments, session, trial, paw and their interaction with

the treatment (saline or muscimol) were considered as fixed effects variables and animal as random effect ($parameter = session * treatment + trial * treatment + paw * treatment + (1|animal)$). Normality of the residuals was verified with D'Agostino's test for mixed linear models. To test for linear relationship between variables, we used Pearson's correlation or linear least-squares regression. To test for differences within a group, between groups or if a group mean is different from zero, we used paired, unpaired or one sample Student's t-test respectively. Normality was tested with D'Agostino's test, homogeneity of variance tested with Levene's test and One-way ANOVA was performed to test the changes in the PSTH AUC for swing length percentiles. Results were considered statistically significant when $p < 0.05$. The main effect and statistical significance are given in the appropriate figure legend. These statistical tests were implemented in custom Python scripts (Python version 3.8) using the Scipy (version 1.8.1) and the Statsmodels (version 0.13.2) modules.

References

Albus, J. S. (1971). A theory of cerebellar function. *Mathematical Biosciences*, *10*(1-2), 25–61. https://doi.org/10.1016/0025-5564(71)90051-4

Arlt, C., & Häusser, M. (2020). Microcircuit Rules Governing Impact of Single Interneurons on Purkinje Cell Output In Vivo. *Cell Reports*, *30*(9), 3020–3035.e3. https://doi.org/10.1016/j.celrep.2020.02.009

Armstrong, D. M., & Edgley, S. A. (1984). Discharges of Purkinje cells in the paravermal part of the cerebellar anterior lobe during locomotion in the cat. *The Journal of Physiology*, *352*, 403–424. https://doi.org/10.1113/jphysiol.1984.sp015300

Armstrong, D. M., Edgley, S. A., & Lidierth, M. (1988). Complex spikes in Purkinje cells of the paravermal part of the anterior lobe of the cat cerebellum during locomotion. *The Journal of Physiology*, *400*, 405–414. https://doi.org/10.1113/jphysiol.1988.sp017128

Armstrong, D. M., & Marple-Horvat, D. E. (1996). Role of the cerebellum and motor cortex in the regulation of visually controlled locomotion. *Canadian Journal of Physiology and Pharmacology*, *74*(4), 443–455. https://doi.org/10.1139/y96-044

Bao, J., Graupner, M., Astorga, G., Collin, T., Jalil, A., Indriati, D. W., Bradley, J., Shigemoto, R., & Llano, I. (2020). Synergism of type 1 metabotropic and ionotropic glutamate receptors in cerebellar molecular layer interneurons in vivo. *eLife*, *9*, e56839. https://doi.org/10.7554/eLife.56839

Barmack, N. H., & Yakhnitsa, V. (2008). Functions of interneurons in mouse cerebellum. *Journal of Neuroscience*, *28*, 1140–1152.

Becker, M. I., & Person, A. L. (2019). Cerebellar Control of Reach Kinematics for Endpoint Precision. *Neuron*, *103*(2), 335–348.e5. https://doi.org/10.1016/j.neuron.2019.05.007

Bellardita, C., & Kiehn, O. (2015). Phenotypic characterization of speed-associated gait changes in mice reveals modular organization of locomotor networks. *Current biology: CB*, *25*(11), 1426–1436. https://doi.org/10.1016/j.cub.2015.04.005

Calame, D. J., Becker, M. I., & Person, A. L. (2023). Cerebellar associative learning underlies skilled reach adaptation. *Nature Neuroscience*, *26*(6), 1068–1079. https://doi.org/10.1038/s41593-023-01347-y

Campagnola, L., Kratz, M. B., & Manis, P. B. (2014). ACQ4: An open-source software platform for data acquisition and analysis in neurophysiology research. *Frontiers in Neuroinformatics*, *8*, 3. https://doi.org/10.3389/fninf.2014.00003

Darmohray, D. M., Jacobs, J. R., Marques, H. G., & Carey, M. R. (2019). Spatial and Temporal Locomotor Learning in Mouse Cerebellum. *Neuron*, *102*(1), 217–231.e4. https://doi.org/10.1016/j.neuron.2019.01.038

Duguid, I., Branco, T., London, M., Chadderton, P., & Hausser, M. (2012). Tonic Inhibition Enhances Fidelity of Sensory Information Transmission in the Cerebellar Cortex. *Journal of Neuroscience*, *32*, 11132–11143. https://doi.org/10.1523/JNEUROSCI.0460-12.2012

Eccles, J. C., Sasaki, K., & Strata, P. (1967). A comparison of the inhibitory actions of Golgi cells and of basket cells. *Experimental Brain Research*, *3*(1), 81–94. https://doi.org/10.1007/BF00234471

Edgley, S. A., & Lidierth, M. (1988). Step-related discharges of Purkinje cells in the paravermal cortex of the cerebellar anterior lobe in the cat. *The Journal of physiology*, *401*(1), 399–415. https://doi.org/10.1113/jphysiol.1988.sp017169

Forli, A., Vecchia, D., Binini, N., Succol, F., Bovetti, S., Moretti, C., Nespoli, F., Mahn, M., Baker, C. A., Bolton, M. M., Yizhar, O., & Fellin, T. (2018). Two-photon bidirectional control and

imaging of neuronal excitability with high spatial resolution in vivo. *Cell Reports*, *22*, 3087–3098. https://doi.org/10.1016/j.celrep.2018.02.063

Franconville, R., Revet, G., Astorga, G., Schwaller, B., & Llano, I. (2011). Somatic calcium level reports integrated spiking activity of cerebellar interneurons in vitro and in vivo. *Journal of neurophysiology*, *106*(4), 1793–805. https://doi.org/10.1152/jn.00133.2011

Gaffield, M. A., & Christie, J. M. (2017). Movement Rate Is Encoded and Influenced by Widespread, Coherent Activity of Cerebellar Molecular Layer Interneurons. *The Journal of Neuroscience*, *37*(18), 4751–4765. https://doi.org/10.1523/JNEUROSCI.0534-17.2017

Gonçalves, A. I., Zavatone-Veth, J. A., Carey, M. R., & Clark, D. A. (2022). Parallel locomotor control strategies in mice and flies. *Current Opinion in Neurobiology*, *73*, 102516. https://doi.org/10.1016/j.conb.2022.01.001

Govorunova, E. G., Sineshchekov, O. A., Janz, R., Liu, X., & Spudich, J. L. (2015). NEUROSCIENCE. Natural light-gated anion channels: A family of microbial rhodopsins for advanced optogenetics. *Science (New York, N.Y.)*, *349*(6248), 647–650. https://doi.org/10.1126/science.aaa7484

Heffley, W., Song, E. Y., Xu, Z., Taylor, B. N., Hughes, M. A., McKinney, A., Joshua, M., & Hull, C. (2018). Coordinated cerebellar climbing fiber activity signals learned sensorimotor predictions. *Nature Neuroscience*, *21*(10), 1431–1441. https://doi.org/10.1038/s41593-018-0228-8

Heiney, S. A., Kim, J., Augustine, G. J., & Medina, J. F. (2014). Precise control of movement kinematics by optogenetic inhibition of Purkinje cell activity. *The Journal of neuroscience : the official journal of the Society for Neuroscience*, *34*(6), 2321–30. https://doi.org/10.1523/JNEUROSCI.4547-13.2014

Hewitt, A. L., Popa, L. S., & Ebner, T. J. (2015). Changes in Purkinje Cell Simple Spike Encoding of Reach Kinematics during Adaption to a Mechanical Perturbation. *Journal of Neuroscience*, *35*(3), 1106–1124. https://doi.org/10.1523/JNEUROSCI.2579-14.2015

Hewitt, A. L., Popa, L. S., Pasalar, S., Hendrix, C. M., & Ebner, T. J. (2011). Representation of limb kinematics in Purkinje cell simple spike discharge is conserved across multiple tasks. *Journal of Neurophysiology*, *106*(5), 2232–2247. https://doi.org/10.1152/jn.00886.2010

Jelitai, M., Puggioni, P., Ishikawa, T., Rinaldi, A., & Duguid, I. (2016). Dendritic excitation-inhibition balance shapes cerebellar output during motor behaviour. *Nature Communications*, *7*. https://doi.org/10.1038/ncomms13722

Kim, J., Lee, S., Tsuda, S., Zhang, X., Asrican, B., Gloss, B., Feng, G., & Augustine, G. J. (2014). Optogenetic mapping of cerebellar inhibitory circuitry reveals spatially biased coordination of interneurons via electrical synapses. *Cell Reports*, *7*, 1601–1613. https://doi.org/10.1016/j.celrep.2014.04.047

Lackey, E. P., Moreira, L., Norton, A., Hemelt, M. E., Osorno, T., Nguyen, T. M., Macosko, E. Z., Lee, W.-C. A., Hull, C. A., & Regehr, W. G. (2023). *Cerebellar circuits for disinhibition and synchronous inhibition* (Preprint). Neuroscience. https://doi.org/10.1101/2023.09.15.557934

Lanore, F., Cayco-Gajic, N. A., Gurnani, H., Coyle, D., & Silver, R. A. (2021). Cerebellar granule cell axons support high-dimensional representations. *Nature Neuroscience*, *24*(8), 1142–1150. https://doi.org/10.1038/s41593-021-00873-x

Lee, K. H., Mathews, P. J., Reeves, A. M. B., Choe, K. Y., Jami, S. A., Serrano, R. E., & Otis, T. S. (2015). Circuit mechanisms underlying motor memory formation in the cerebellum. *Neuron*, *86*(2), 529–540. https://doi.org/10.1016/j.neuron.2015.03.010

Lopes, G., Bonacchi, N., Frazão, J., Neto, J. P., Atallah, B. V., Soares, S., Moreira, L., Matias, S., Itskov, P. M., Correia, P. A., Medina, R. E., Calcaterra, L., Dreosti, E., Paton, J. J., & Kampff, A. R. (2015). Bonsai: An event-based framework for processing and controlling data streams. *Frontiers in Neuroinformatics*, *9*, 7. https://doi.org/10.3389/fninf.2015.00007

Lyu, C., Yu, C., Sun, G., Zhao, Y., Cai, R., Sun, H., Wang, X., Jia, G., Fan, L., Chen, X., Zhou, L., Shen, Y., Gao, L., & Li, X. (2022). Deconstruction of Vermal Cerebellum in Ramp Locomotion in Mice. *Advanced Science (Weinheim, Baden-Wurttemberg, Germany)*, *10*(1), e2203665. https://doi.org/10.1002/advs.202203665

Machado, A. S., Darmohray, D. M., Fayad, J., Marques, H. G., & Carey, M. R. (2015). A quantitative framework for whole-body coordination reveals specific deficits in freely walking ataxic mice. *eLife*, *4*(OCTOBER2015). https://doi.org/10.7554/eLife.07892

Mapelli, L., Pagani, M., Garrido, J. A., & D'Angelo, E. (2015). Integrated plasticity at inhibitory and excitatory synapses in the cerebellar circuit. *Frontiers in Cellular Neuroscience*, *9*. https://doi.org/10.3389/fncel.2015.00169

Marple-Horvat, D. E., & Criado, J. M. (1999). Rhythmic neuronal activity in the lateral cerebellum of the cat during visually guided stepping. *The Journal of Physiology*, *518*(2), 595–603. https://doi.org/10.1111/j.1469-7793.1999.0595p.x

Marr, D. (1969). A theory of cerebellar cortex. *The Journal of Physiology*, *202*(2), 437–470. https://doi.org/10.1113/jphysiol.1969.sp008820

Mathis, A., Mamidanna, P., Cury, K. M., Abe, T., Murthy, V. N., Mathis, M. W., & Bethge, M. (2018). DeepLabCut: Markerless pose estimation of user-defined body parts with deep learning. *Nature Neuroscience*, *21*(9), 1281–1289. https://doi.org/10.1038/s41593-018-0209-y

Mittmann, W., Koch, U., & Hausser, M. (2005). Feed-forward inhibition shapes the spike output of cerebellar Purkinje cells. *J Physiol*, *563*, 369–378.

Musall, S., Kaufman, M. T., Juavinett, A. L., Gluf, S., & Churchland, A. K. (2019). Single-trial neural dynamics are dominated by richly varied movements. *Nature Neuroscience*, *22*(10), 1677–1686. https://doi.org/10.1038/s41593-019-0502-4

Ozden, I., Dombeck, D. A., Hoogland, T. M., Tank, D. W., & Wang, S. S. H. (2012). Widespread State-Dependent Shifts in Cerebellar Activity in Locomoting Mice. *PLoS ONE*, *7*, e42650. https://doi.org/10.1371/journal.pone.0042650

Pasalar, S., Roitman, A. V., Durfee, W. K., & Ebner, T. J. (2006). Force field effects on cerebellar Purkinje cell discharge with implications for internal models. *Nature Neuroscience*, *9*(11), 1404–1411. https://doi.org/10.1038/nn1783

Roome, C. J., & Kuhn, B. (2014). Chronic cranial window with access port for repeated cellular manipulations, drug application, and electrophysiology. *Frontiers in Cellular Neuroscience*, *8*, 379. https://doi.org/10.3389/fncel.2014.00379

Sauerbrei, B. A., Lubenov, E. V., & Siapas, A. G. (2015). Structured Variability in Purkinje Cell Activity during Locomotion. *Neuron*, *87*(4), 840–852. https://doi.org/10.1016/j.neuron.2015.08.003

Sawtell, N. B. (2017). Neural Mechanisms for Predicting the Sensory Consequences of Behavior: Insights from Electrosensory Systems. *Annual review of physiology*, *79*(1), 381–399. https://doi.org/10.1146/annurev-physiol-021115-105003

Sedaghat-Nejad, E., Pi, J. S., Hage, P., Fakharian, M. A., & Shadmehr, R. (2021). *Synchronous spiking of cerebellar Purkinje cells during control of movements* (Preprint). Neuroscience. https://doi.org/10.1101/2021.09.16.460700

Vinueza Veloz, M. F., Zhou, K., Bosman, L. W. J., Potters, J.-W., Negrello, M., Seepers, R. M., Strydis, C., Koekkoek, S. K. E., & De Zeeuw, C. I. (2015). Cerebellar control of gait and interlimb coordination. *Brain structure & function*, *220*(6), 3513–36. https://doi.org/10.1007/s00429-014-0870-1

Acknowledgements

We thank Dr. Isabel Llano for careful reading and feedback on the manuscript. We thank Drs. Kishore Kuchibhotla, Florent Haiss and David DiGregorio for their insightful comments on the manuscript. This study was supported by the 'Agence National de la Recherche' (ANR, project : "WalkingCrossingNeurons", ANR-18-CE37-0006-01; and project: "FrontCog", ANR-17-EURE-0017), and an EMBO postdoctoral fellowship to Heike Stein (ALTF 471-2021). We acknowledge the use of the animal services at BioMedTech Facilities (INSERM US 36, CNRS UMS 2009, Université Paris Cité). We thank Patrice Jegouzo and Thierry Bastien of the mechanical workshop at BioMedTech Facilities for manufacturing parts of the LocoReach setup. We thank Sandrine El Marhomy (Université Paris Cité, CNRS, SPPIN, Paris, France) for managing the mice colony and for genotyping.

Author Contributions Statement

M.G. conceived and designed the study. M.G. and J.G. built the setup and performed first pilot experiments. A.A. carried out the experiments presented here. A.J. conducted the post mortem histology. A.A., C.B. and M.G. carried out the analysis. H.S. and N.A.C.G. contributed the GLM analysis. M.G., A.A., H.S. and N.A.C.G. discussed results, interpreted the data and wrote the manuscript. M.G. supervised the project.

Competing Interests Statement

The authors declare no competing interests.

Supplementary Information

Cerebellar interneuron activity is triggered by reach endpoint during learning of a complex locomotor task

Andrianarivelo *et al.* 2023

A. Supplementary figures

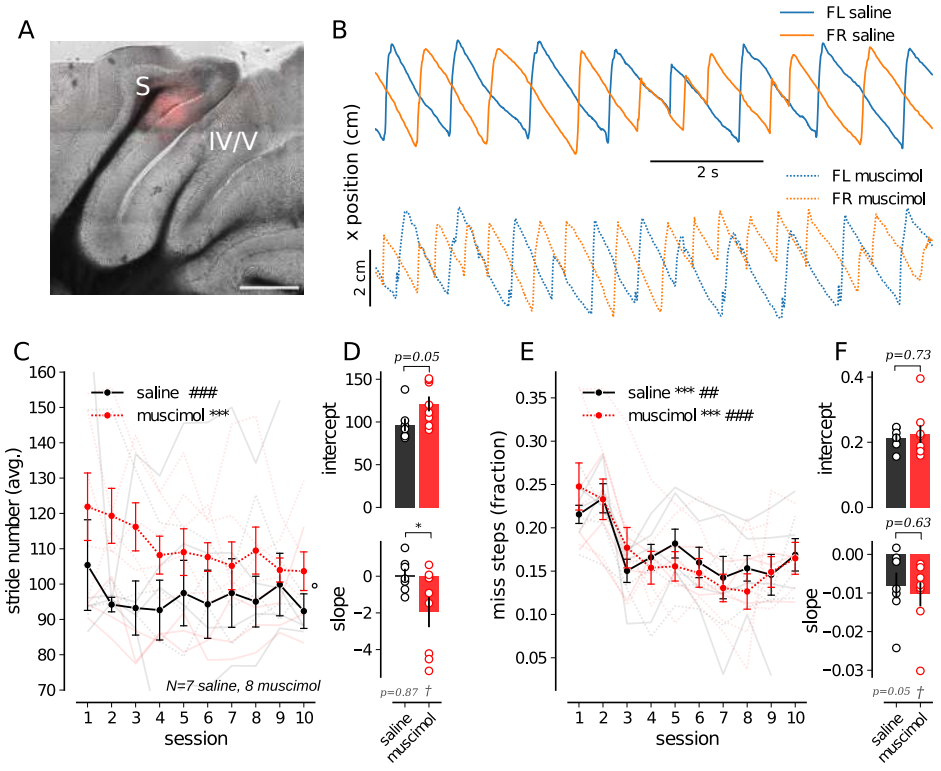

Figure A.1: Muscimol inactivation of lobulus simplex affects walking performance. Fluorophore-conjugated muscimol or saline were perfused in 16 mice 30 min before each session. Infusion location and spread was verified histologically after the last behavioral session. We reduced the imposed baseline wheel speed for this set of experiments to lower the difficulty of the task for the muscimol/saline-infused animals (5.8 cm/s compared to 7.5 cm/s above). (**A**) Photomicrograph showing spread of fluorophore-conjugated muscimol in a coronal cerebellar section. Lobulus simplex (S) and lobule IV/V of the vermis are marked (scale bar : 500 μm). (**B**) FL (blue) and FR paw (orange) x-positions during a sample period of a single trial for a saline (top, full lines) and a muscimol-infused animal (bottom, dashed lines). The following mean behavioral parameters are shown for muscimol- (red, $N = 8$) and saline- (black, $N = 7$) infused animals : (**C**) stride number across sessions (saline, session effect: $C = -0.061$, $p = 0.7821$, trial effect: $C = -1.94$, $p < 0.0001$; muscimol, session effect: $C = -1.665$, $p < 0.0001$, trial effect: $C = -0.906$, $p = 0.076$, treatment effect: $C = 1.653$, $p = 0.047$), (**D**) stride number across sessions linear fit intercept (top, unpaired Student's t-test, $t = -2.108$, $P = 0.054$, saline vs muscimol) and slope (bottom, unpaired Student's t-test, $t = -2.162$, $P = 0.049$, saline vs muscimol; one sample Student's t-test, $t = 0.17$, $p = 0.867$ for saline vs 0, $t = -2.398$, $p = 0.047$ for muscimol vs 0) of individual muscimol- and saline-infused animals, (**E**) fraction of miss steps across sessions (saline, session effect: $C = -8.843$, $p < 0.0001$, trial effect: $C = -3.16$, $p = 0.002$; muscimol, session effect: $C = -0.010$, $p < 0.0001$, trial effect: $C = -0.007$, $p = 0.001$, treatment effect: $C = 0.002$, $p = 0.542$), and (**F**) fraction of miss steps linear fit intercept (top, unpaired Student's t-test, $t = -2.108$, $P = 0.054$, saline vs muscimol) and slope (bottom, unpaired Student's t-test, $t = -2.162$, $P = 0.049$, saline vs muscimol; one sample Student's t-test, $t = -2.417$, $p = 0.052$ for saline vs 0, $t = -3.292$, $p = 0.013$ for muscimol vs 0). Data are presented as mean ± SEM over ten sessions. Statistical significance was determined by a Linear Mixed Model. The regression coefficient (C) and corresponding p-value are reported for behavioral parameters across sessions. $^*p < 0.05$, $^{**}p < 0.01$, $^{***}p < 0.0001$ effect of sessions. $\#p < 0.05$, $\#\#p < 0.01$, $\#\#\#p < 0.0001$ in-between trials effect. $^\circ p < 0.05$, $^{\circ\circ}p < 0.01$ treatment effect. For linear fit parameters comparisons, statistical significance was determined by an unpaired or one sample Student's t-test. $\star p < 0.05$ saline vs muscimol, † $p < 0.05$ muscimol vs 0 (grey).

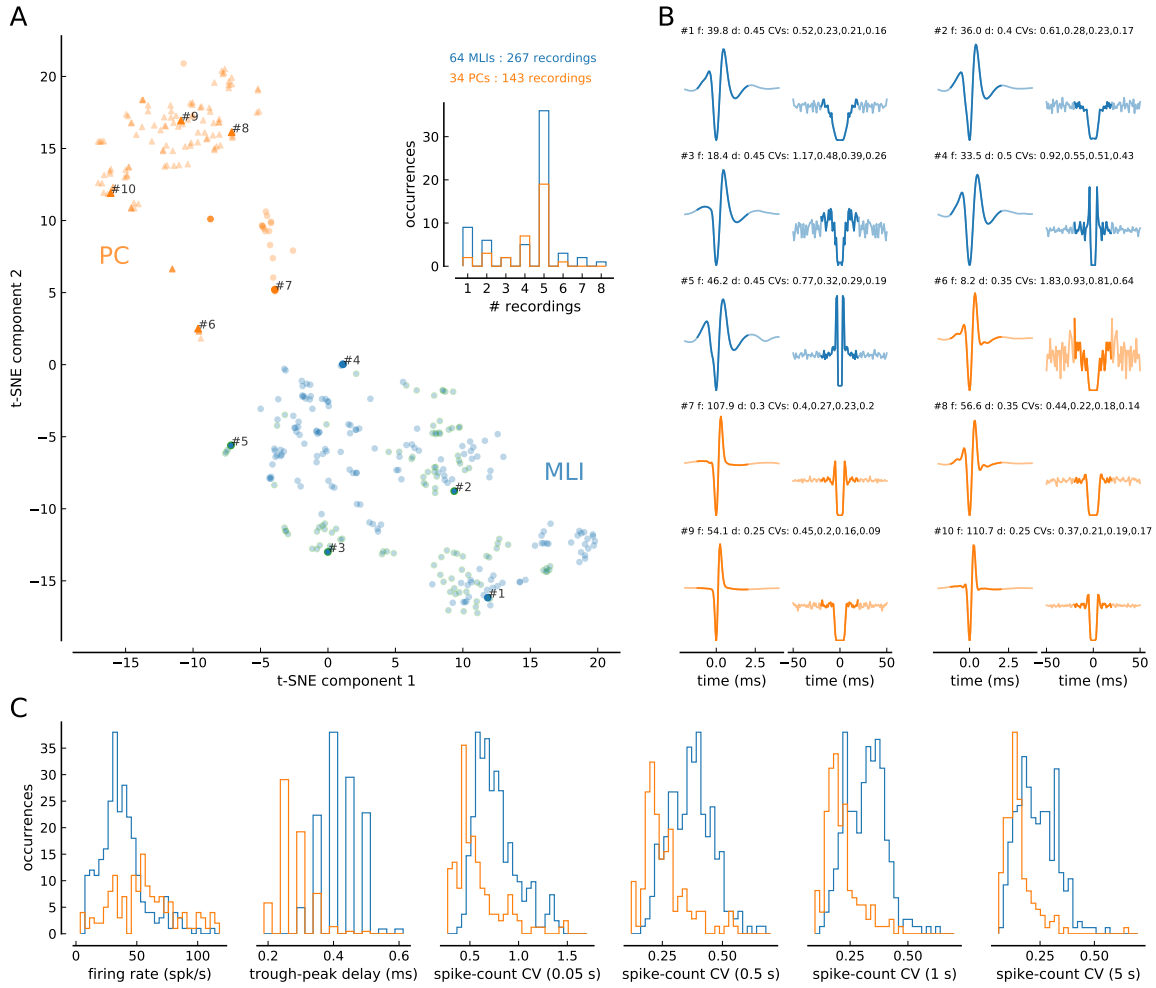

Figure A.2: Clustering of all recorded cells with t-distributed Stochastic Neighbor Embedding (t-SNE). (**A**) All recordings are shown based on their first two t-SNE components. t-SNE converts similarities between data points to joint probabilities and tries to minimize the Kullback-Leibler divergence between the joint probabilities of the low-dimensional embedding and the high-dimensional data. For the t-SNE dimensionality reduction, the spike-waveform, the autocorrelogram, the firing rate, the trough-to-peak delay of the waveform, the spike-count coefficient of variation for four different bin sizes (0.05, 0.5, 1 and 5 s), and the existence or not of complex spikes are used as input parameters. Blue symbols are identified as MLIs and orange as PCs. Triangles indicate cells with complex spikes. Symbols with green edge were visually identified during the recording. The inset shows histograms of the number of recordings (trials) performed for all cells in each populations. (**B**) Average spike waveform (left) and autocorrelgogram (right) for ten example cells. The examples are marked in panel (A). Firing rate, f, in spk/s and the trough-to-peak delay, d, in ms and the spike-count coefficient of variation for four different bin sizes (0.05, 0.5, 1 and 5 s) are shown for each cell (top of the panel). The portion of the curves used for the t-SNE dimensionality reduction is shown in bold color. (**C**) Histograms of other parameters used in the dimensionality reduction. Each measure is shown for MLIs (blue) and PCs (orange). From left to right : firing rate, trough-to-peak delay of the aveage spike waveform, and the spike-count coefficient of variation for four different bin sizes : 0.05, 0.5, 1 and 5 s.

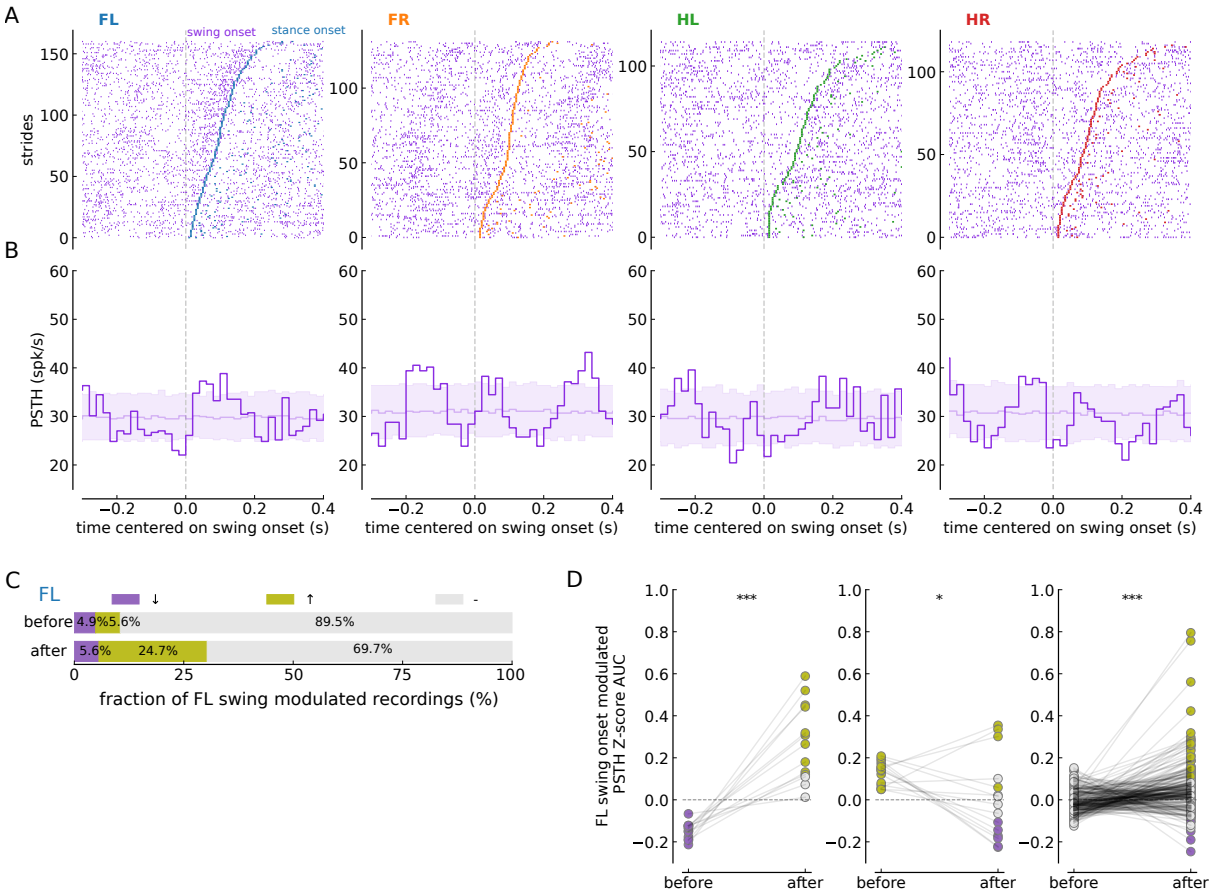

Figure A.3: Swing onset-aligned MLI activity modulations. Similar depiction as in Fig. 5 but for swing-onset alignment. (**A**) Raster plots showing the occurrence of spikes aligned to swing onset (vertical gray dashed lines) during all strides of each paw (four columns for FL, FR, HL and HR from left), for an example recording of an MLI. Strides are sorted by swing duration. Ordered, colored ticks at positive times mark stance onset time for the swing starting at 0 s, and the following tick marks swing onset for the subsequent swing. (**B**) Swing-onset aligned PSTH corresponding to each paw's raster plot shown in (A). Pale purple lines and shaded area are mean and $[5, 95]$ percentile intervals of 300 swing-onset aligned PSTHs with shuffled spikes times (see Methods for details). (**C**) For the FL paw, the faction of significantly up (↑), down (↓), or not (−) modulated MLIs before- and after swing onset. The criterion for sig. modulation is two consecutive crossings of the $[5, 95]$ percentile interval of shuffled PSTHs during the 100 ms before or after swing onset. (**D**) The area under the z-scored PSTH curve (AUC) before and after FL swing-onset separated by before-down (left panel), before-up (middle) and before-not (right) modulated cells. The AUC before and after swing-onset of the same cells are connected with gray lines (paired Student's t-test; $^*p < 0.05$, $^{***}p < 0.0001$ before vs after). All results is in this figure are based on individual recordings.

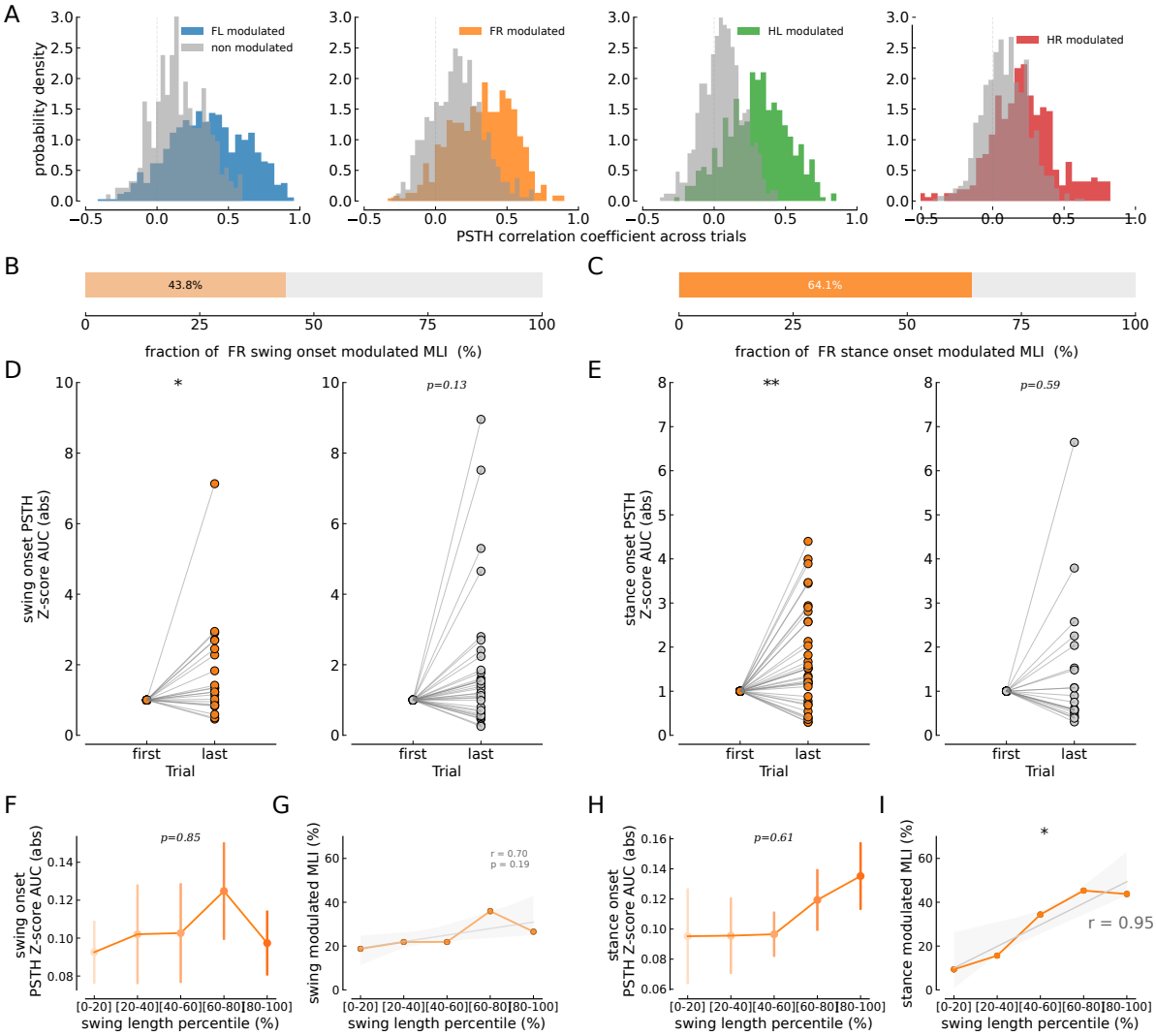

Figure A.4: Across-trial FR paw swing- and stance onset-aligned MLI activity. Same depiction as in Fig. 6 but for FR paw (except for (A)). (**A**) Pearson correlation between PSTHs of different trails of a given cell. The distribution of correlations is shown for all four paws (panels from left to right), for modulated cells (in color) and for non-modulated cells (grey). (**B,C**) Fraction of MLIs with at least one or more trials with significant modulations around FR swing (B) or stance (C) onset. (**D,E**) The area under the z-scored PSTH curve (AUC) around FR swing onset (D) and FR stance onset (E) is shown for the last trial relative to the first trial of modulated (left panel) and non-modulated (right panel) cells (analysis window $[-100, 100]$ ms; paired Student's t-test, p-values reported in the panels). (**F,H**) Absolute AUC for swing (F, one-way ANOVA, $F = 0.336$, $p = 0.852$) and stance onset (H, one-way ANOVA, $F = 0.679$, $p = 0.607$) of cells modulated for a given range of swing length percentile. (**G,I**) Fraction of swing onset (G) and stance onset (I) modulated MLIs for ranges of FR paw swing length percentiles (Linear regression analysis, correlation coefficient r, and the significance of the regression p are reported in the panels). Significance is marked according to $^*p < 0.05$, $^{**}p < 0.01$, $^{***}p < 0.001$.

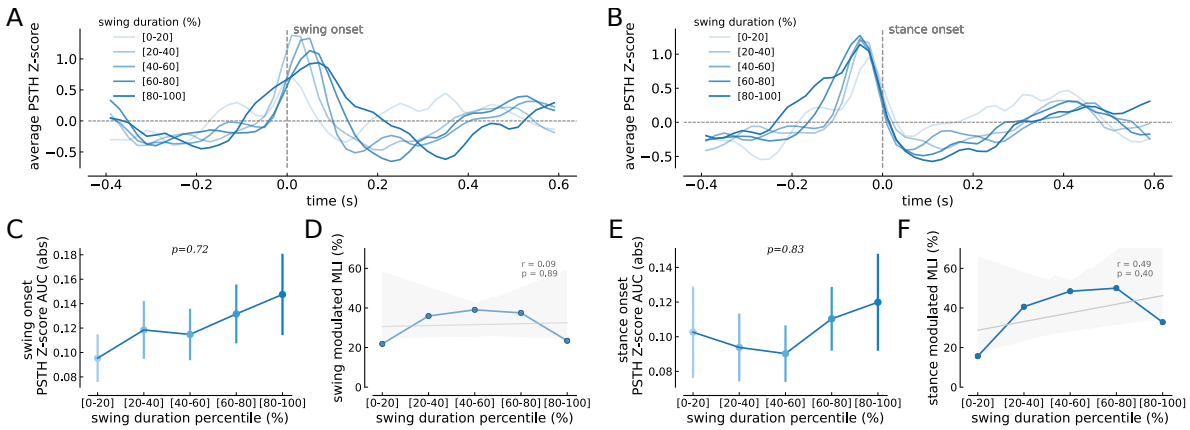

Figure A.5: Across-trial FL paw swing- and stance onset-aligned MLI activity for stride durations ranges. Could the change in activity modulation across trials be related to the fact that swings become more stereotyped, since swing duration is less variable later in the session (Fig. 2G,H)? Here, we computed the firing rate modulation strength and the fraction of modulated cells based for swings falling within defined ranges of swing durations during one session (swing duration percentile-based analysis). (**A, B**) Average FL swing (A) and stance (B) onset-aligned, z-scored PSTH of significantly modulated MLIs for increasing ranges of swing length percentiles. (**C,E**) AUC for swing (C, one-way ANOVA, $F = 0.519$, $p = 0.721$) and stance onset (E, one-way ANOVA, $F = 0.374$, $p = 0.83$) of cells modulated for a given range of swing duration percentile. (**D,F**) Fraction of swing onset (D) and stance onset (F) modulated MLIs for ranges of swing duration percentiles (Linear regression analysis, correlation coefficient r, and the significance of the regression p are reported in the panels). Significance is marked according to $^*p < 0.05$, $^{**}p < 0.01$, $^{***}p < 0.001$. In summary, neither the activity modulation magnitude nor the fraction of modulated cells depended on the swing duration across trials. Interestingly, the peak of the average swing-onset aligned PSTH for modulated cells shifts with the swing length (A), highlighting the fact that the activity modulation is linked to swing end and not the beginning.

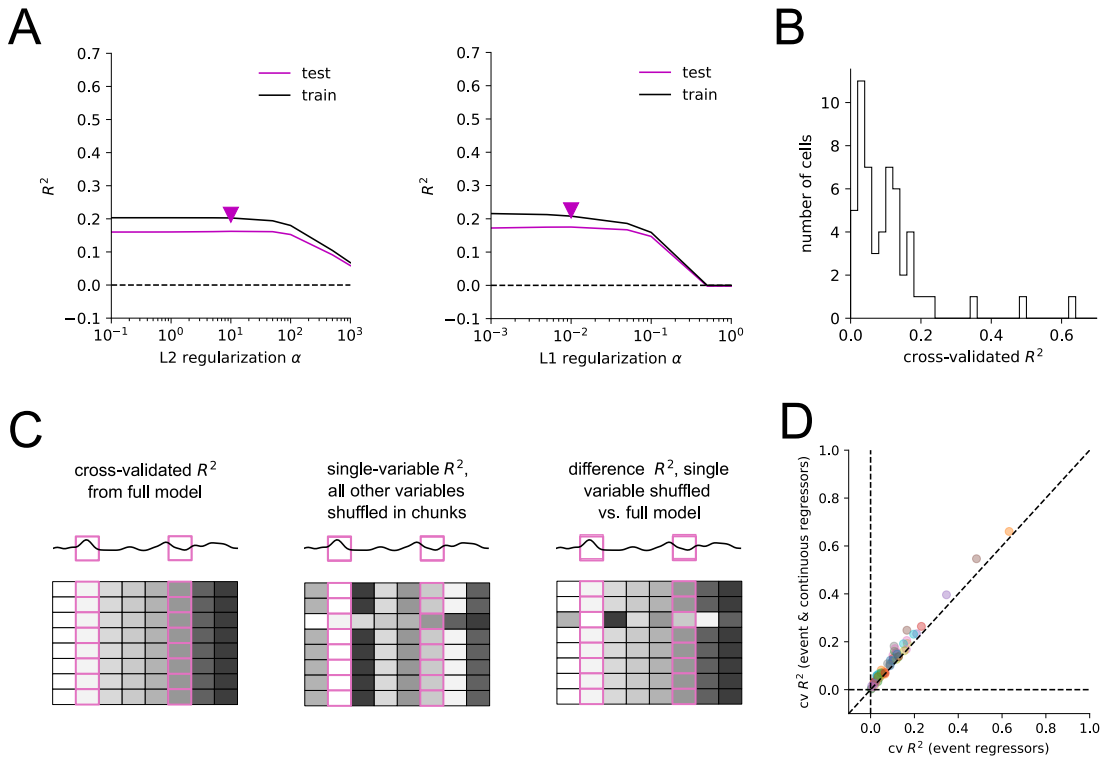

Figure A.6: GLM analysis approach and R^2 quantifications. (**A**) Illustration of how the regularization weight α is determined for both, the L2 and the L1-regularized regressions. The change of train and test R^2 is shown as function of the regularization weight α, for an example regression. We used the largest value of α before a considerable drop in R^2 as indicated by the arrow. (**B**) Histogram of the cross-validated R^2s for the full model with 8 regressors (swing/stance onset for FL, FR, HL, and HR) after the second L2-regularized regression for all cells. (**C**) Cross-validated R^2 from the full model (left), from single-variable model (middle), and from a leave-one-variable-out model (right). In all models, we cut time series into decorrelated chunks of 200 ms bins (Methods), trained the GLM on 80% of chunks, and assessed the R^2 on the left-out 20% of chunks. For single-variable models, we shuffled the chunks of all other variables before training to keep only the relationship between firing rates and the variable of interest. To assess the unique contribution of the variable of interest, we calculated the difference in R^2 after shuffling the variable of interest vs. the R^2 in the full model. Significance was determined based on 95% confidence intervals from 100 repeated shuffles. (**D**) Comparison of the cross-validated R^2 between the regression model with 8 regressors (swing/stance onset for FL, FR, HL, and HR) and a model with the 8 event regressors plus the continuous variables, *i.e.*, the four paw positions, paw speeds and the wheel speed.